SAND REPORT

SAND2002-4014
Unlimited Release
Printed January 2003

Solidification Diagnostics for Joining and Microstructural Simulations

Charles V. Robino and Aaron C. Hall
Joining and Coating Department

J. A. Brooks
Engineered Materials Department

Thomas J. Headley
Materials Characterization Department

Allen Roach
Multiphase Transport Processes Department

Sandia National Laboratories
Albuquerque, NM 87185-0889 and Livermore, CA 94550

Prepared by
Sandia National Laboratories
Albuquerque, New Mexico 87185 and Livermore, California 94550

Sandia is a multiprogram laboratory operated by Sandia Corporation,
a Lockheed Martin Company, for the United States Department of Energy's
National Nuclear Security Administration under Contract DE-AC04-94-AL85000.

Issued by Sandia National Laboratories, operated for the United States Department of Energy by Sandia Corporation.

Available to DOE and DOE contractors from
U.S. Department of Energy
Office of Scientific and Technical Information
P.O. Box 62
Oak Ridge, TN 37831

Telephone: (865)576-8401
Facsimile: (865)576-5728
E-Mail: reports@adonis.osti.gov
Online ordering: http://www.doe.gov/bridge

Available to the public from
U.S. Department of Commerce
National Technical Information Service
5285 Port Royal Rd
Springfield, VA 22161

Telephone: (800)553-6847
Facsimile: (703)605-6900
E-Mail: orders@ntis.fedworld.gov
Online order: http://www.ntis.gov/help/ordermethods.asp?loc=7-4-0#online

SAND2002-4014
Unlimited Release
Printed January 2003

Solidification Diagnostics for Joining and Microstructural Simulations

Charles V. Robino and Aaron C. Hall
Joining and Coating Department

J. A. Brooks
Engineered Materials Department

Thomas J. Headley
Materials Characterization Department

Allen Roach
Multiphase Transport Processes Department

Sandia National Laboratories
Albuquerque, NM 87185-0889 and Livermore, CA 94550

Abstract

Solidification is an important aspect of welding, brazing, soldering, LENS fabrication, and casting. The current trend toward utilizing large-scale process simulations and materials response models for simulation-based engineering is driving the development of new modeling techniques. However, the effective utilization of these models is, in many cases, limited by a lack of fundamental understanding of the physical processes and interactions involved. In addition, experimental validation of model predictions is required.

We have developed new and expanded experimental techniques, particularly those needed for in-situ measurement of the morphological and kinetic features of the solidification process. The new high-speed, high-resolution video techniques and data extraction methods developed in this work have been used to identify several unexpected features of the solidification process, including the observation that the solidification front is often far more dynamic than previously thought. In order to demonstrate the utility of the video techniques, correlations have been made between the in-situ observations and the final solidification microstructure. Experimental methods for determination of the solidification velocity in highly dynamic pulsed laser welds have been developed, implemented, and used to validate and refine laser welding models. Using post solidification metallographic techniques, we have discovered a previously unreported orientation relationship between ferrite and austenite in the Fe-Cr-Ni alloy system, and have characterized the conditions under which this new relationship develops. Taken together, the work has expanded both our understanding of, and our ability to characterize, solidification phenomena in complex alloy systems and processes.

Contents

List of Figures

List of Tables

Introduction

Solidification is an important aspect of materials processing and fabrication. Examples of interest to Sandia National Laboratories include: welding, brazing, soldering, LENS fabrication, and casting. Solidification affects, and often controls, the structure and properties of alloys in their final application. Current trends toward large-scale materials and process simulations and model-based engineering are driving development of new modeling techniques. However, effective utilization of these models and simulations is limited, in large part, by insufficient understanding of the physical processes and interactions involved in the solidification process. In particular, solidification in alloys based on the Fe-Cr-Ni ternary system has been of significant interest for many years. Nevertheless, many aspects of its solidification are not understood in sufficient detail to support development and effective utilization of high performance simulations. In this report we discuss work that attempts to expand and refine our mechanistic descriptions of solidification in general and in an important alloy system specifically. We have focused on two principal approaches; in-situ observations of the solidification process, and detailed post-solidification metallographic analyses.

The first of these approaches resulted in the development of high-speed, high-resolution video techniques for visualization of the solidification front. This approach can provide quantitative measurements of key process features, can be used to further develop mechanistic descriptions of the solidification process, and provides for direct validation of solidification models. The basic features of the technique and several examples of its application are presented in the body of this report.

The second approach, detailed metallographic analyses of Fe-Cr-Ni alloy solidification, resulted in the discovery of a previously unreported orientation relationship between ferrite and austenite in these alloys. This observation was completely unexpected, and demonstrates the utility of thorough metallographic assessments. Moreover, the observation suggests that, in spite of many years of study by investigators throughout the world, solidification in this important alloy system is not fully understood. It is believed that the observations discussed here will form the basis for more refined mechanistic descriptions of solidification in Fe-Ni-Cr based alloys.

Overview Of Visualization Techniques

Background

It is difficult to characterize solidification phenomena in welds because of the intense heat, high speeds, and small sizes involved. Conventional experimental techniques for characterizing solidification phenomena in welds involve rapidly quenching the weld pool and examining the quenched microstructure. Visualization techniques have been investigated as an alternative method of characterizing solidification phenomena in welds. Using a high quality zoom lens and a high-speed CCD camera the solid-liquid interfaces in a number of welds were filmed at high magnification. Both the trailing (solidifying) edge and the leading (melting) edge of the weld pool were filmed. Computer image analysis techniques were developed and used to extract quantitative information from these images. These experimental techniques were then used to investigate weld rippling phenomenon in Gas Tungsten Arc (GTA) welds and to measure solidification velocities in laser spot welds.

High-speed video-microscopy allows large amounts of information about the solid-liquid interface to be accessed under actual welding conditions. At low magnification, the dendritic structure of the solid-liquid interface can be clearly observed, as can characteristic ripples caused by pool instabilities. At higher magnification, secondary dendrite arms can be seen protruding through the liquid surface of the weld pool. Other solidification related phenomena can also be captured including: melting, weld ripple formation, and fluid flow. Significant information about the evolution and structure of the solid-liquid interface can be extracted from video clips using computerized image analysis techniques. This information can be directly related to the microstructure of the finished weld.

High-speed, high-magnification video microscopy was used to investigate rippling behavior in autogenous 304 stainless steel GTA welds. Images of the trailing edge of a weld pool (solid-liquid interface) were collected during the welding process. Weld ripple formation was observed and the associated solid-liquid interface velocity was measured. A distinct sequence of events was observed each time a ripple formed. This sequence of events involved apparent changes in the solid-liquid interface velocity, dendrite morphology, and dendrite growth direction.

The microstructures of a group of rippled welds were examined and a number of features associated with the rippling phenomenon were identified. These features included changes in the pattern of the interdendritic constituents and changes in the solute distribution across the ripple feature. This information coupled with the video images was used to better explain weld rippling phenomenon and the origins of microstructural changes associated with it. It was shown that solute redistribution occurs in the weld on a length scale associated with the ripple features.

Visualization techniques were also used to characterize the laser spot welding process. Laser spot welding is a common technique for joining small components that require precise fit-up and small distortion after joining. Finite element models of the laser spot welding process are being developed so that more effective welds can be made. The models being developed use an arbitrary Lagrangian / Eulerian finite element method to predict the formation of the keyhole and

the solidification velocities in the laser spot weld. These velocity predictions evolve from the recoil pressure caused by rapid evaporation from the high temperature molten surface and the thermal boundary conditions. The recoil pressure is used as a boundary condition to determine the deformation of the free surface of the molten pool. High-speed, high-magnification video microscopy experiments have been used to measure solidification velocities in actual laser spot welds. Solidification velocity data were extracted from video clips using computerized image analysis software. This data was compared to computer model predictions of solidification velocity. This comparison allowed for validation of the fluid and thermal boundary conditions used in the finite element model.

Visualization Techniques

Conventional experimental schemes for investigating solid-liquid interfaces (drop furnaces and tin quenching) (Brooks, Yang et al. 1993; Huang, Inatomi et al. 1997; DuPont, Robino et al. 1998) are based on rapidly cooling a partially liquid sample. The quenching process "freezes in" the solid-liquid interface, which is then studied metallographically. Experimental techniques based on such schemes are very useful but have a significant limitation. They only provide the researcher with a "snapshot" of the solid-liquid interface. No direct information about the motion or the evolution of the solid-liquid interface is available from a quenching experiment. This information is critical in order to fully understand the solidification phenomenon.

The only experimental schemes that do provide information about the motion and the evolution of the solid-liquid interface are based on visualization of transparent materials (like succinonitrile) that solidify in a manner analogous to metals (Glicksman, Koss et al. 1995; Glicksman, Koss et al. 1995; Glicksman, Koss et al. 1996). These experiments have provided a wealth of information about dendrite growth and the evolution of the solid-liquid interface. Creating solidification conditions in a polymer that are representative of the conditions that occur in an engineering material being welded is difficult if not impossible. In addition, polymer analogues often do not exhibit the complex solidification phenomena seen in metals. Solidification mode transformations, which are commonly observed in stainless steels (Elmer, Allen et al. 1989), are an example of complex phenomena that are not exhibited by transparent materials. Complex phenomena like this demand new experimental techniques that can provide information about the dynamic behavior of solid-liquid interfaces in engineering materials.

The most straightforward solution to this problem is to image the solid-liquid interface in-situ and use those images to track its motion and evolution. A number of experimental schemes are being developed for in-situ investigation of solid-liquid interfaces (Orrling, Fang et al. 1999; Orrling, Fang et al. 2001). Many of these schemes are based on confocal scanning laser microscopy. High magnification video imaging provides similar quality images with considerably simpler equipment.

A new experimental scheme based on high-speed, high-magnification video imaging of the solid-liquid interface in a GTA weld will be discussed below. First a number of still images taken from videos of the solid-liquid interface will be shown. The features in the image that define the solid-liquid interface will be related to the microstructure of the weld. Next, an

example illustrating the extraction of quantitative data from such a video will be discussed. Finally, a few cautions concerning the investigation of solid-liquid interfaces using this technique will be presented.

Visualization Procedures

The video images reported in this document were captured using two different high-speed cameras: a Kodak® EktaPro and a Speed Vision HGTX 2000. A Navitar® Zoom 6000 lens was used with each camera. The Kodak camera is capable of capturing digital images at up to 12,000 frames / second. The Speed Vision camera is capable of capturing images at up to 2000 frames / second. The images from the Speed Vision camera are significantly higher resolution than the images from the older Kodak camera. The Navitar lens is designed specifically for machine vision. It is a parafocal zoom lens system capable of imaging objects within fields of view ranging from 146.6mm to 0.03mm. The camera and weld torch are fixed with respect to each other and the sample is translated below them as shown in Figure 1. This arrangement keeps the solid-liquid interface stationary with respect to the camera. Shielding is necessary to prevent oxide from forming on the surface of the weld pool and obscuring the solid-liquid interface. Welds can be made at a variety of amperage, arc length, and speed combinations. Solidification and melting phenomena are filmed by pointing the camera at locations on the edge of the weld pool.

Lighting is of critical importance even around a welding arc. Digital cameras have a limited dynamic range for a given exposure; however, the exposure can typically be varied

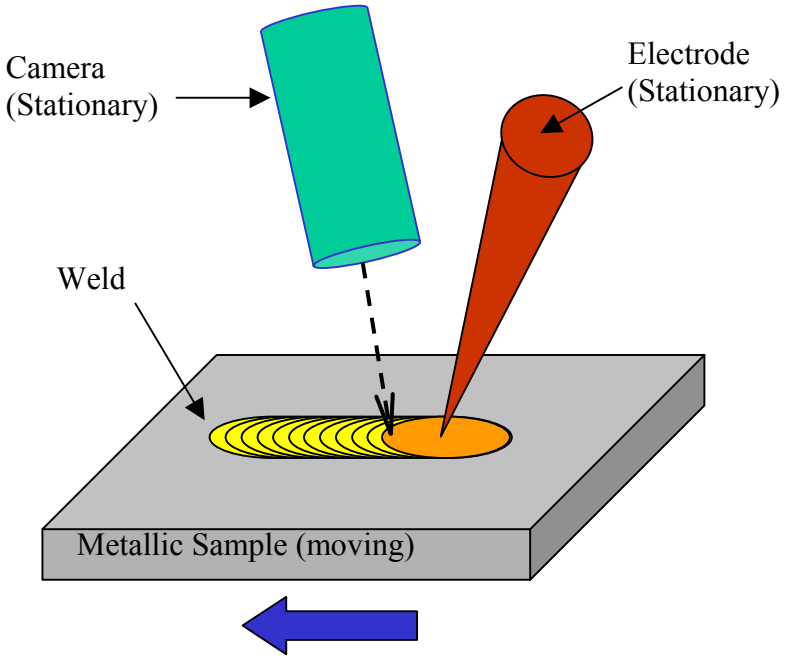

Figure 1. Schematic showing the arrangement of the camera, sample, and welding torch.

considerably. As a result, total image contrast becomes an issue, not light intensity. Thus, successfully capturing images near an intense light source, like a welding arc, requires reduction of the contrast in the scene. This is accomplished by lighting the scene with extremely bright lights (similar intensity to the welding arc). Once the contrast is reduced the exposure can be adjusted so that the entire scene can be viewed.

Interpreting Images of a GTA Weld

Figure 2 shows two still images of the advancing solid-liquid interface in a 150-amp DC gas tungsten arc (GTA) weld traveling at 4.2 mm/sec in 304 stainless steel. The advancing solid-liquid interface can be seen in Figure 2a at relatively low magnification. Dendrite-like structures can be seen at the solid-liquid interface. Figure 2b is an image of the same interface taken at higher magnification. The linear dendrite like features in Figure 2a can now be resolved as rows of dots at the liquid surface. These dots are thought to be secondary dendrite arms penetrating the liquid surface. Solidified welds were further investigated to verify this. Two SEM images of the solidified surface are shown in Figure 3. The dot-like features seen in the video closely correlate in arrangement and spacing to the features seen on the solidified surface.

The images in Figure 4 show the microstructure of this weld. Figure 4a is a transverse cross section, Figure 4b is a central longitudinal cross section. The dots seen in Figure 3 also appear in Figure 4a. The spacing between the dots in Figure 4a is approximately 30 microns. This is somewhat larger than the primary arm spacing suggested in the video because the dendrite growth direction at this location is not perpendicular to the polished surface of the sample (see Figure 5). Figure 5 is a diagram showing the location of the images with respect to the weld. Both the primary and secondary arm spacing can be seen in Figure 4b. In this case, the dendrite growth direction is parallel to the polished surface of the sample. The primary arm spacing is approximately 20 microns and the secondary arm spacing is 10 microns. Clearly the dot like features observed at the solid-liquid interface in the video can be associated with dendrite arms penetrating the liquid surface.

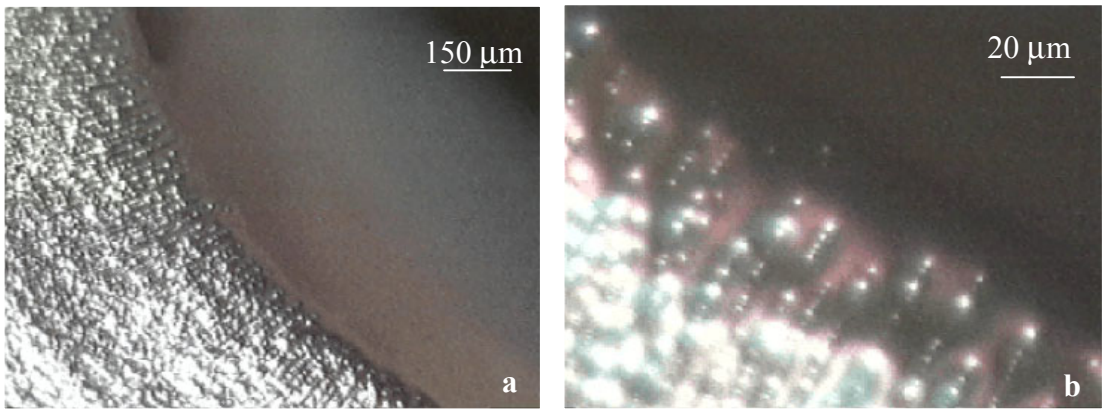

Figure 2. Low and high magnification images of the solid-liquid interface in a GTA weld.

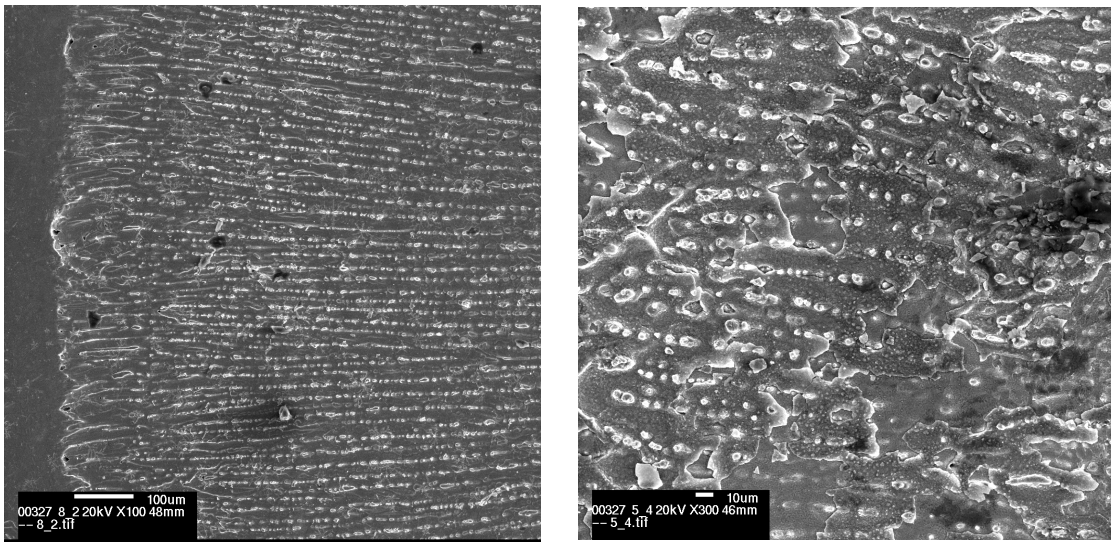

Figure 3. SEM images of the as-solidified weld surface. Evidence of a weld ripple can be seen on the left side of the image. Rows of secondary dendrite arms can be seen protruding from the rest of the surface.

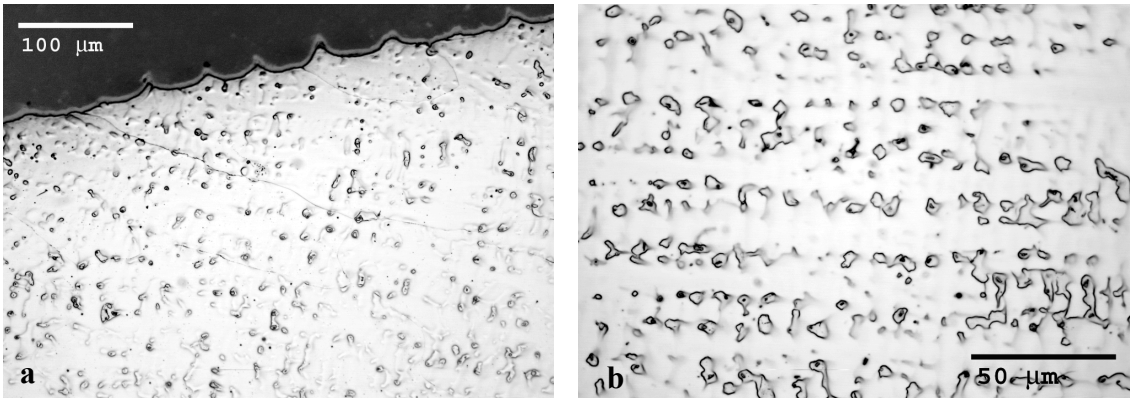

Figure 4. Metallographic cross sections of the weld showing that the dots on the solidified surface can be associated with dendrites.

Data Extraction

Over the last decade, significant advances have been made in digital photography and related computer technology. Combination of these technologies has given rise to a field known as machine vision. It is now relatively straightforward to capture and process images using a computer. Robust software exists that allows the user to extract quantitative measurements from digital images. This technology has found widespread application in the world's manufacturing industries (Babb 1995; Hogarth 1999; Zuech 2000). Parts are routinely inspected using machine vision technology to see that they have been assembled properly or manufactured to desired tolerances. Surprisingly, this technology has not been widely adopted in the scientific community. It affords the researcher with a powerful new tool set that allows large amounts of

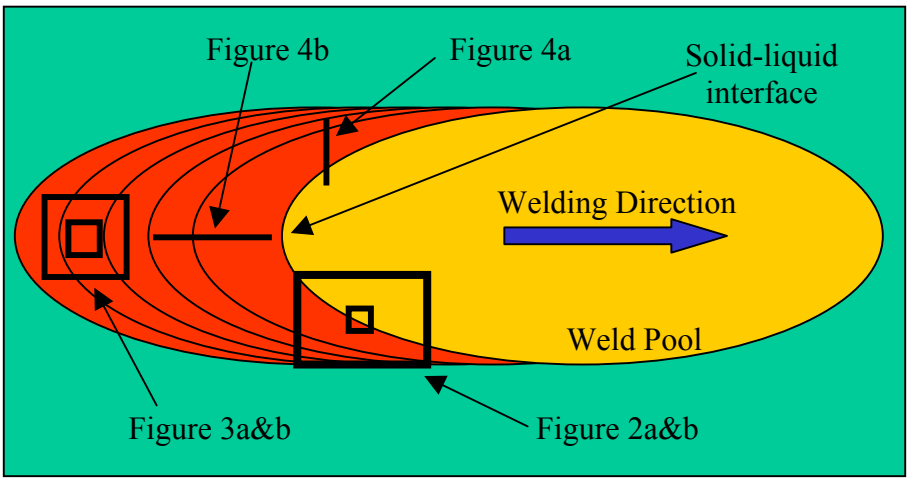

Figure 5. Diagram showing the locations of Figure 2, 3, and 4 with respect to the weld pool. The dendrite growth direction is normal to the solid-liquid interface.

information about dynamic physical processes to be accessed and extracted in an automated fashion. Solidification of metals is a field that is ripe for the exploitation of such technology.

Interface velocity, primary dendrite arm spacing, and secondary dendrite arm spacing can be measured from a video using computerized image analysis. High-magnification videos are useful for studying the behavior of the solid-liquid interface. Lower magnification videos are useful for measuring interface velocities during solidification. Figure 6 shows a still image taken from a video of a solidifying GTA spot-weld in stainless steel.

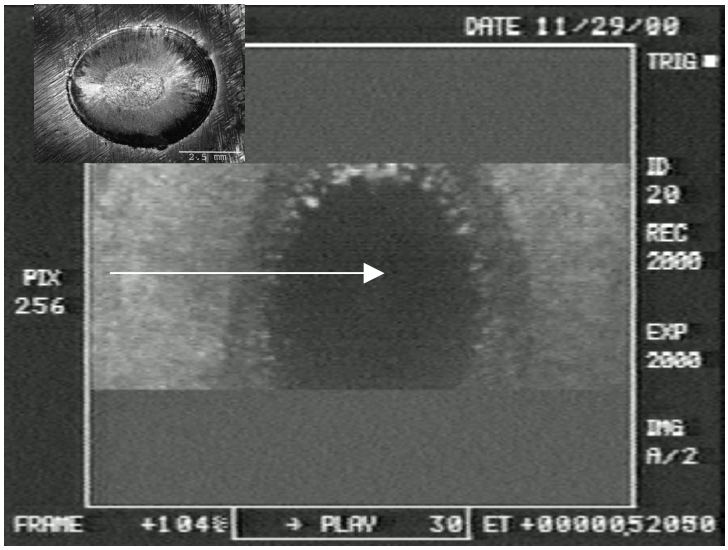

Figure 6. Solidifying 75 Amp GTA spot-weld in stainless steel. The inset shows the solidified weld. The arrow marks the location where the data in Figure 7 was extracted.

We have extracted interface velocity versus time data from this video by measuring the interface position in each frame of the video. This was accomplished using National Instruments® Lab View and IMAQ Vision software. Because the frame rate of the camera is known, a curve showing interface position versus time can be generated. The slope of this curve is then calculated to yield a velocity measurement. Figure 7 shows the data extracted from the spot-weld video.

Two relatively constant velocity regimes were observed in this weld. As solidification progresses and the liquid pool gets smaller the apparent solidification velocity appears to increase sharply from 1.2 mm/s to 1.7 mm/s. This type of high-resolution measurement of interface velocity is expected to be useful for verifying thermal boundary conditions in solidification-based models of welding processes. In an earlier paper we described a visualization-based measurement of changes in solid-liquid interface velocity associated with a weld ripple (Hall, Robino et al. 2001). Those changes were correlated with microstructural features that extended throughout the depth of the weld.

Figure 8 is a still image taken from a video of a 150 amp GTA weld in 304 stainless steel traveling at 4.2 mm/sec. Dendrites can be seen at the solid-liquid interface. Figure 9 is a still image showing melting in Inconel 718. Liquation of the interdendritic laves and/or niobium carbide eutectic-like constituents can be seen at the solid-liquid interface. Figure 10 is a still image showing weld ripples in 304 stainless steel. Multiple weld ripples can be seen behind the solid-liquid interface.

A large amount of information about the solid-liquid interface and its motion with time is present in these video recordings. Quantitative information can be extracted from these video clips in a relatively straightforward manner using computerized image analysis schemes.

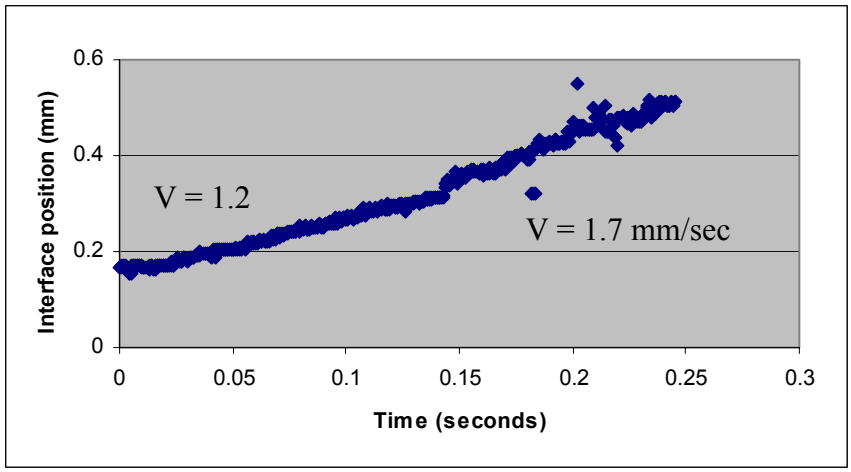

Figure 7. Data extracted from the spot weld shown in Figure 5.Interface position in the X-direction is measured and plotted with respect to time.

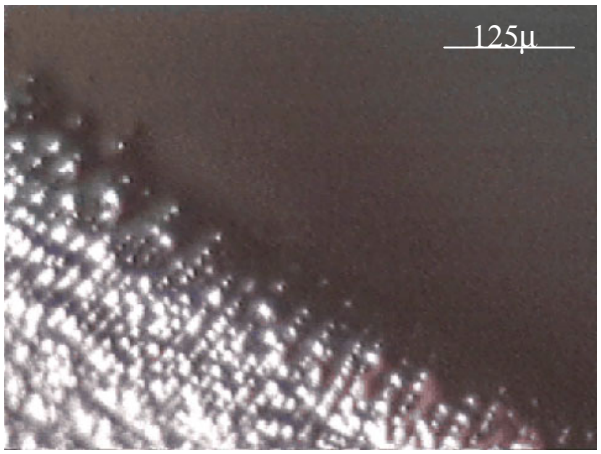

Figure 8. Dendrites at the solid-liquid interface in a GTA weld in 304 stainless steel.

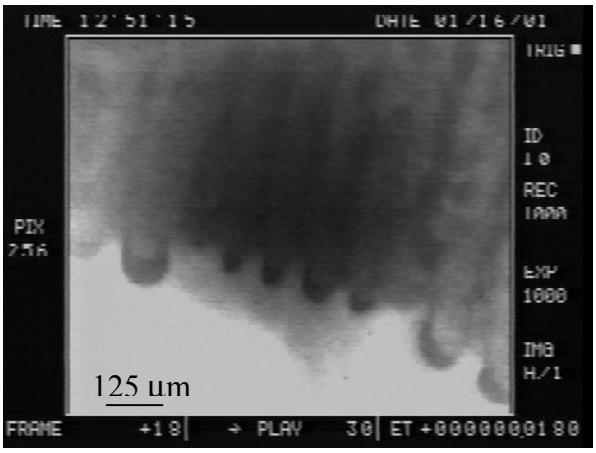

Figure 9. Melting at the solid-liquid interface in Inconel 718, liquation can be seen at the interface.

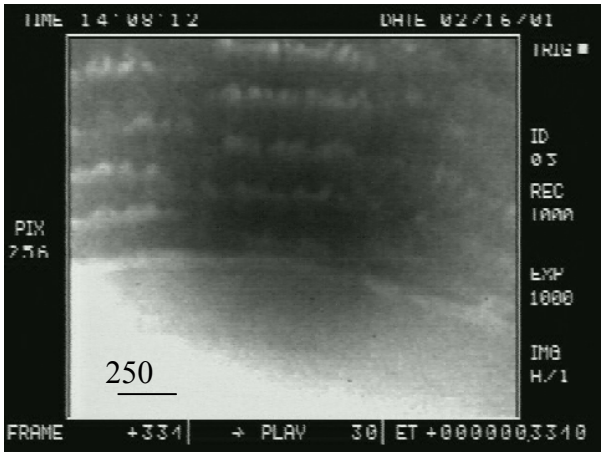

Figure 10. Weld ripples at the trailing edge of a GTA weld in 304 stainless steel.

Our image analysis scheme proceeds as follows. First, a digital movie is recorded as a series of image files. Each movie typically contains between one and two thousand image files each of which are 500KB in size. Image analysis software is used to open each image file in sequence and measure a feature of interest (a dendrite arm spacing, the location of an interface, etc…). All measurements are made in a pixel coordinate system that uses the top left corner of the image as an origin. After each measurement is made, it is associated with the frame number of the image and written to an output file. Frame number and pixel coordinates must then be converted into meaningful units like time and position. Frame number is easily translated into time by multiplication with the framing rate. A dimensional measurement like primary arm spacing requires a simple unit conversion to an appropriate length measurement. Filming an accurate scale provides this, as well as a velocity calibration. A measurement like interface velocity requires a frame of reference correction in addition to a unit conversion. A frame of reference correction is necessary because all measurements are made in the camera frame of reference. If information like interface velocity is to be translated into the sample frame of reference, the stage velocity must be measured accurately and accounted for.

In the video that Figure 10 was extracted from the motion of the solid-liquid interface that is associated with the formation of a weld ripple was seen. That motion was quantified by measuring the position of the solid-liquid interface in each frame of the video. The interface position is determined from a marked intensity change in the digital image. Figure 11 is a graph of this information. The upper curve shows interface position in pixels coordinates with respect

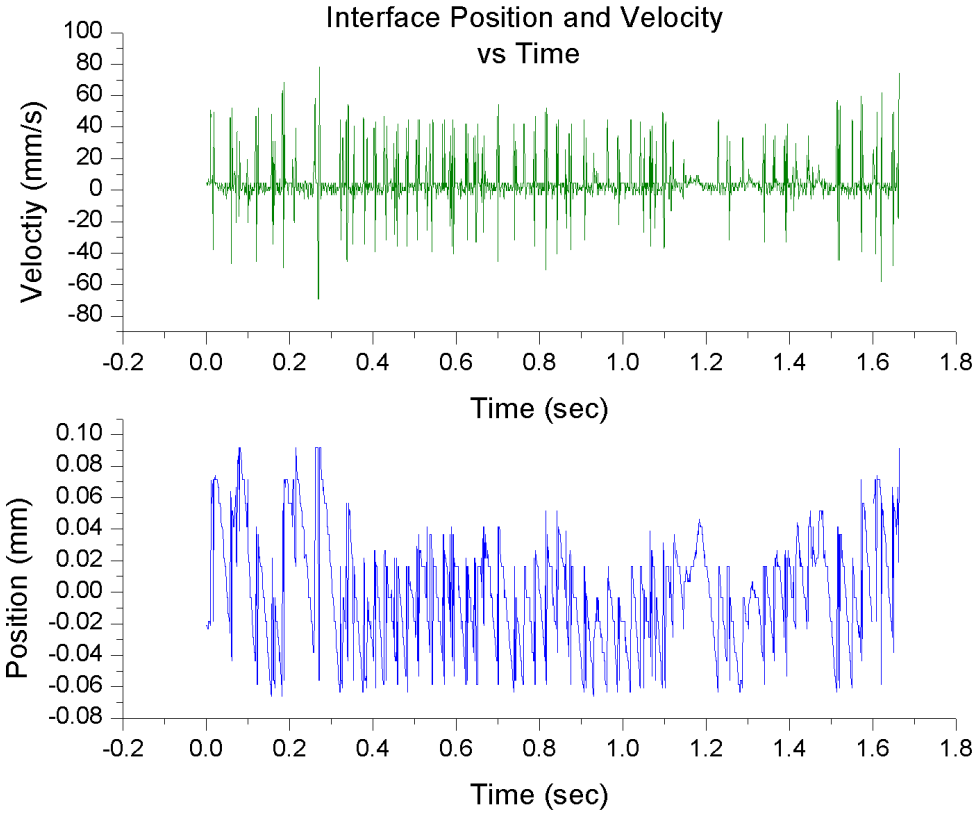

Figure 11. Interface position (lower curve) and interface velocity (upper curve) obtained from high-speed video of a rippling weld.

to time. The interface behavior associated with the formation of a weld ripple can now be clearly seen. When a ripple is formed the solid-liquid interface appears to go thorough a cycle of advancing and remelting.

Evidence of this change in interface velocity can be seen in the microstructure of the finished weld. Figure 12 is a micrograph showing the transverse cross section of a rippled weld in 304 stainless steel. Light colored bands in the shape of the solid-liquid interface can be seen in the image. Similar features can be seen in longitudinal cross sections of rippled welds. These features are associated with the ripple formation seen in the video. As shown in Figure 12, the ripple bands extend all the way to the bottom of the weld pool. Like the metallographic cross section shown in Figure 12, the video clips mentioned above are two-dimensional representations of three-dimensional phenomena. Microstructural evidence of cyclic interface motion deep within the weld pool suggests that data gathered at the surface of the pool can be correlated with phenomena that occur deeper in the pool.

Considerations

The example given above illustrates how machine vision technology can be used to measure the solid-liquid interface velocity associated with weld ripple formation. It allowed the solid-liquid interface velocity to be measured with high temporal resolution. A cyclic solid-liquid interface velocity was observed and was associated with microstructural features present throughout the depth of the weld. This suggested that data collected from this type of experiment can provide limited information about phenomena deep within a weld pool. By applying the same technique to the other videos mentioned above, primary and secondary dendrite arm spacings, and local melting velocities can also be measured as a function of time and welding conditions. Clearly machine vision has tremendous potential as a data collection technique for scientific experiments. This potential is not limited to solidification science; in fact machine vision could be used to study almost any dynamic phenomena. In the case of

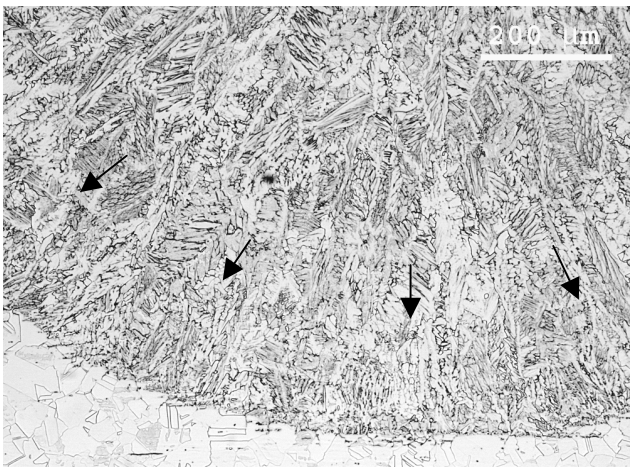

Figure 12. Cross section of a GTA weld showing evidence of rippling in the microstructure.

solidification science it has allowed us to view and quantitatively measure the dynamic behavior of the solid-liquid interface in an engineering material under actual welding conditions.

As with any experimental scheme, there are potential pitfalls. The primary and secondary arm spacing measurements, suggested in the video mentioned initially, do correlate with the spacings measured in the sample. Despite this, interpretation of the features in a video like this should be done with caution. Weld visualization gives us access to a tremendous amount of information however that information is only accessed at the surface of the weld pool. Like a metallographic section these images are a two-dimensional view of a three-dimensional phenomena. Close examination of Figure 4(a) suggests that the bumps on the solidified surface are secondary dendrite arms. It also suggests that the primary dendrite arms are not necessarily parallel to the liquid surface. This presents a potential pitfall for the extraction of individual dendrite velocities. While weld visualization techniques do provide a wealth of information about the solid liquid interface, they do not provide any direct information about the solid-liquid interface deep within the pool because the molten metal obscures the interface at that location. Any conclusions about the evolution, motion, velocity, or dendrite spacings within the pool must be inferred from the features visible at the surface of the pool. In many cases these associations are appropriate, as illustrated above, nevertheless they should be made with appropriate caution.

In the sections that follow, two detailed examples of the application of visualization techniques are presented. The first is a detailed characterization of the association of microstructural features and rippling phenomenon in 304 stainless steel welds. The second discusses use of the visualization technique for laser spot weld model validation.

Association of Microstructural Features and Rippling Phenomenon in 304 Stainless Steel Gas Tungsten Arc Welds

Introduction

Weld rippling is a phenomenon common to many welding processes. It affects weld microstructure and may be useful as a basis for penetration control (Andersen, Cook et al. 1997; Aendenroomer and denOuden 1998). A better understanding of weld rippling phenomenon, its relationship to weld microstructure, and its origins will contribute to the preparation of better quality welds.

Weld ripples are the arc-shaped topographic features on the surface of solidified weld beads. These arc-shaped features are associated with the prior solid-liquid interface of the weld. Typically, they extend across the entire weld bead and are oriented with their concave side in the direction of the weld travel as shown in Figure 13.

Weld ripples can be observed in the solidified metal produced by essentially all known traveling heat source welding processes. Many authors have investigated the origins of weld ripples (D'annessa 1970; Garland and Davies 1970; Kotecki, Cheever et al. 1972; Ecer, Gokhale et al. 1980; Mazumder 1991; Postacioglu, Kapadia et al. 1991; Morvan and Bournot 1996; Wei, Chang et al. 1996). A number of different formation mechanisms have been identified

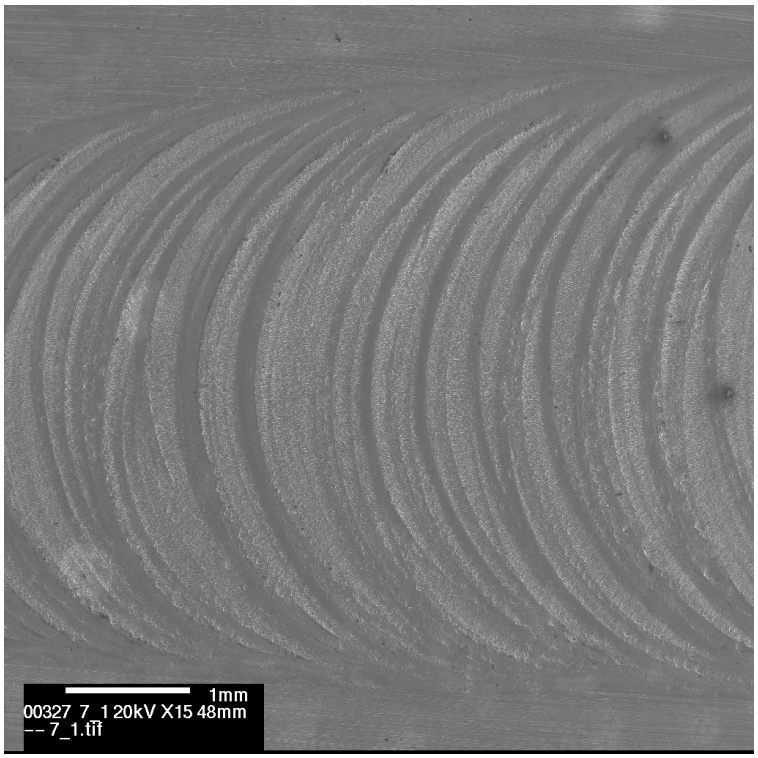

Figure 13. An SEM image of the surface of a DC GTA weld in 304 stainless steel. The heat source traveled from left to right across the image. The arc shaped undulations on the surface of this weld are weld ripples.

depending on the welding process and the geometry of the weld in question. These mechanisms fall into three general categories: 1) solidification related phenomena (D'annessa 1970); 2) vibration related phenomena (Garland and Davies 1970; Kotecki, Cheever et al. 1972; Ecer, Gokhale et al. 1980; Postacioglu, Kapadia et al. 1991) and; 3) fluid flow related phenomena (Mazumder 1991; Morvan and Bournot 1995; Wei, Chang et al. 1996; Nemchinsky 1997).

Very few of these investigators describe the rippling phenomenon itself or the microstructural changes associated with it. This paper will focus on describing these features of weld ripples. High-speed, high-resolution video-microscopy is used to provide a detailed description of the weld-rippling phenomenon. Measurements of the apparent solid-liquid interface velocity associated with weld ripple formation is included in this description. Next, a detailed examination of the microstructure of these welds is presented. Specific changes in interdendritic material, grain orientation, and local chemistry have been detected and are described. These changes are correlated with the high-speed, high-magnification video images to create a more complete description of weld rippling phenomenon and its effect on weld microstructure.

Experimental Procedures

Video Microscopy

The solid-liquid interface in a GTA weld was filmed using a Kodak EktaPro camera equipped with a Navitar® Zoom 6000 lens. The Kodak camera is capable of capturing digital images at up to 12,000 frames / second. In practice, we have found that filming at 2000 frames / second provides a temporal resolution that is more than adequate for a GTA weld at the travel speeds investigated. The Navitar lens is designed specifically for machine vision. It is a parafocal zoom lens system capable of imaging objects within fields of view ranging from 146.6mm to 0.03mm on each side. The camera and welding torch were fixed with respect to each other. The sample was translated below them, (see Figure 1), so that the solid-liquid interface is approximately stationary with respect to the camera. A laminar flow GTA torch and a 90% Ar - 10% He gas mixture was used to shield the weld. This prevented oxide from forming on the surface of the weld pool and obscuring the solid-liquid interface. All welding coupons were 3 mm X 25 mm X 165 mm AISI 304 stainless steel coupons. All welds were made using a Weldcraft GTA torch and Miller Maxstar 152 welding power source operating at 75 amps AC. The sample was traversed under the torch using a motion control stage equipped with Compumotors (Model S57-102-MO-E) traveling at 4.2 mm/sec (10 inches / minute). An Ar-10%He mixture was used as a shielding gas.

Quantitative information was extracted from the video clips using National Instruments™ Lab View® and IMAQ Vision® software. Our image analysis scheme was as follows. First, a digital movie was recorded as a series of Tiff image files. Each movie typically contained between one and two thousand image files. Image analysis software was used to open each image file in sequence and measure the location of the solid-liquid interface. All measurements were made in a pixel coordinate system. After each measurement was made, it was associated with the frame number of the image and written to an output file. Frame number and pixel coordinates were then converted into meaningful units, such as time and position. Frame number

was translated into time by multiplication with the framing rate. Dimensional measurements required a simple unit conversion to an appropriate length measurement. This was accomplished by filming an accurate scale marker, which also provided a velocity calibration. A measurement like interface velocity requires a frame of reference correction, in addition to a unit conversion. A frame of reference correction was necessary because all measurements were made in the camera frame of reference. Interface velocity was translated into the sample frame of reference by accounting for the stage velocity.

Metallography

Longitudinal and transverse sections of rippled welds were prepared and examined in the optical microscope. A Vickers micro-hardness indenter was used to mark the visible ripples so that they could be located during subsequent analysis.

Automated crystal orientation mapping was performed on polished surfaces of the weld samples. The maps were obtained in a JEOL 5900LV scanning electron microscope equipped with a ThermoNoran ORKID electron backscattered diffraction (EBSD) system for orientation mapping. Orientation maps were collected by scanning the electron beam pixel-by-pixel across the area of interest. At each pixel, an EBSD pattern was collected, and automatically indexed and the orientation calculated. The orientations were displayed using colors to represent different orientations (Schwartz, M et al. 2000).

Electron microprobe analysis (EPMA) was used to document the composition changes across the ripple features noted in the polished samples. These procedures included small step sizes between analytical points and long count times at high current and voltage. Thus, it was possible to distinguish compositional variations due to the weld ripples from those due to microsegregation at the size scale of dendrites.

All samples were examined using a JEOL 8600 Electron Microprobe X-ray Analyzer. First, a necessary, ultra-thin layer of carbon was evaporated on the polished sample surfaces to conduct excess electrons off the surface when exposed to the electron beam in the probe. Then Energy Dispersive Spectroscopy (EDS) was performed to identify the elements present in the sample. Sometimes this was augmented with higher resolution Wavelength Dispersive Spectrometry (WDS) to resolve ambiguities. The major alloy constituents, Cr, Fe, and Ni, and the minor constituents, Si, Mn, Co, Cu, and Mo, were tracked. Trace elements such as C, O, P, and S were not tracked because they were not abundant enough to help resolve the composition variations associated with the weld ripple.

Analytical conditions that produced minimal error due to counting statistics were used because we suspected that any composition variations due to the weld ripple would be subtle and super-imposed on sharp variations due to dendritic growth. An excitation voltage of 25 KeV was used since this voltage is capable of fully exciting the X-rays for all of the alloying elements present. In addition high current (50 nA) and long count times (120 sec.) on the WDS spectrometers were used to yield large counts, thereby keeping the counting statistical error small. All eight elements were analyzed in the event that one of the minors was especially good at defining the composition differences. Every element analyzed was calibrated against a pure

metal standard under the same beam conditions. Small step sizes of 1 to 3 μm were used because the composition variations caused by dendrites were at the 10 to 30μm scale, while the composition variations caused by the weld-ripple were much broader, making the two easily distinguishable.

Results and Discussion

Video Microscopy

The advancing solid-liquid interface in a DC GTA weld in 304 stainless steel was filmed. Figure 14 is a series of high magnification images showing the formation of an individual weld ripple. The weld travel direction is from the top of the image to the bottom of the image. This sequence of images captures a distinct series of events that was observed each time a ripple formed. The first event in the ripple formation cycle is an apparent reduction of the solid-liquid interface velocity. This event is captured in images (a) and (b). Notice that in image (a) the solid-liquid interface is near the bottom of the image. Fifty milliseconds later in image (b) the solid liquid interface is near the top of the image. Since the sample is moving at a constant rate

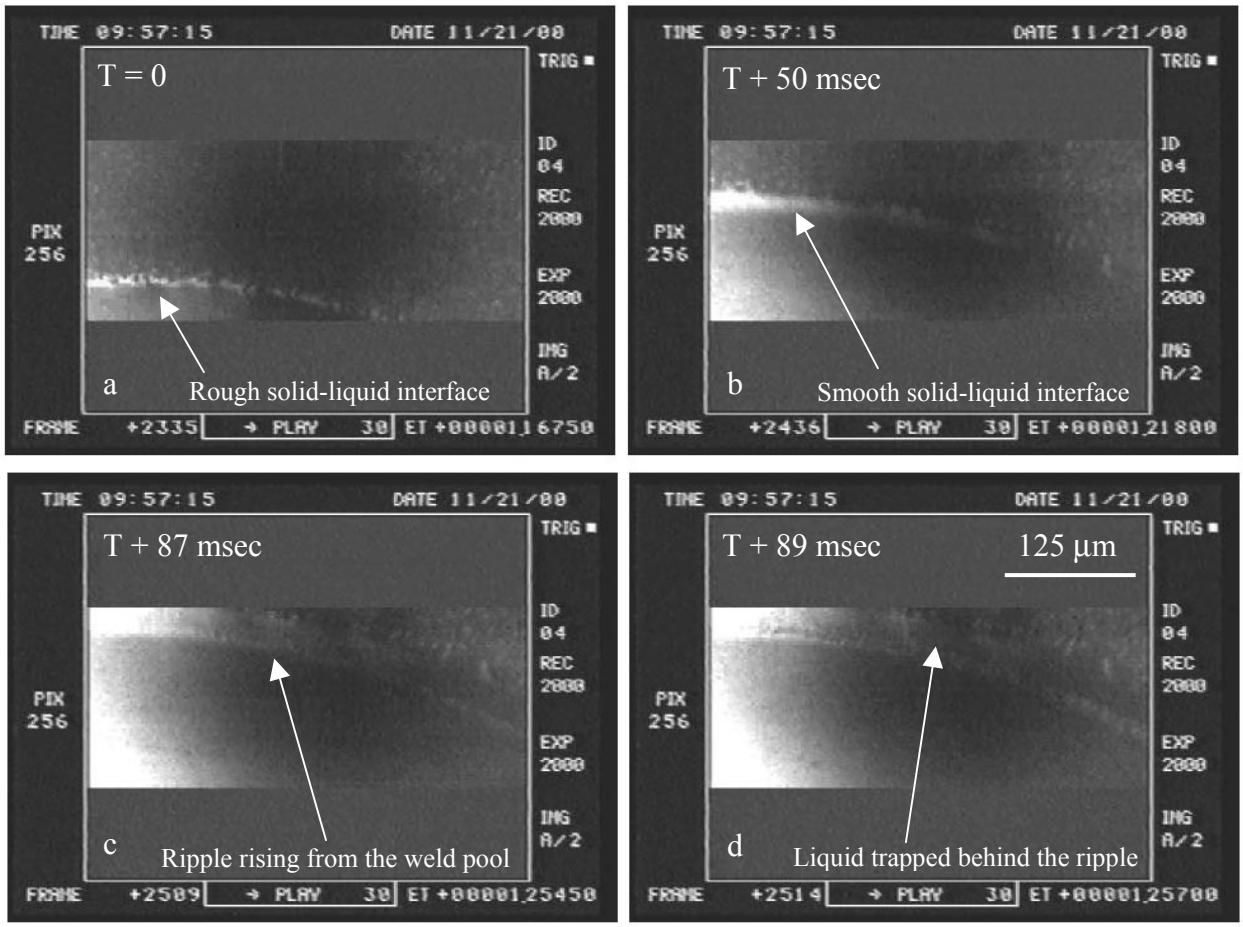

Figure 14. High-speed, high-magnification video sequence showing the formation of an individual weld ripple.

with respect to the camera, the motion suggests that the interface has slowed down. The second event is the disappearance of the dendritic structure visible at the solid-liquid interface. This occurs as the interface appears to slow. Notice that, in image (a) the solid-liquid interface has a well defined dendritic structure and in image (b) the interface is relatively smooth. The third event is the movement of a perturbation along the length of the solid-liquid interface perpendicular to the weld travel direction (i.e. around the circumference of the pool). This perturbation is difficult to see in the still images but can be clearly seen in the video. It moves very quickly, traversing the entire field of view in approximately 2.5 milliseconds. The last event in the sequence is the growth of the ripple feature. In Figure 14(c-d), the ripple feature can be seen, apparently rising from the melt pool. A small amount of liquid is trapped behind the ripple and can be seen solidifying in Figure 14(d). If the ripple is rising from the pool, part of the solid-liquid interface must be growing in a direction perpendicular to the travel direction of the weld. After the ripple has risen from the weld pool, the growth direction again appears parallel to the weld travel direction and the ripple formation cycle begins again.

The apparent solid-liquid interface velocity in a lower magnification video was measured using computer image analysis software. Figure 11 shows the results of these measurements. The frequency of the velocity change is ~ 75Hz, and the interface velocity varies from a maximum of 47 mm/sec to a minimum of – 40 mm/sec. As expected, the average velocity (4.7 mm/sec) is approximately equal to the stage velocity (4.2 mm/sec). This suggests that the pool volume is not changing during an individual ripple event. The interface velocity appears to fluctuate over a large range, even becoming negative. This suggests that the growing interface actually retreats (remelts) during part of the rippling cycle. This is consistent with the video images shown in Figure 14. Melting would explain the disappearance of the dendrite-like features observed during the ripple formation cycle.

In our experiment, the camera is fixed with respect to the tungsten electrode and we observe a cyclic change in the position of the solid liquid interface. Three modes of pool behavior could result in this observation. They are schematically represented in Figure 15. Consider a free liquid (the weld metal) in a container (the solid base material). The first mode

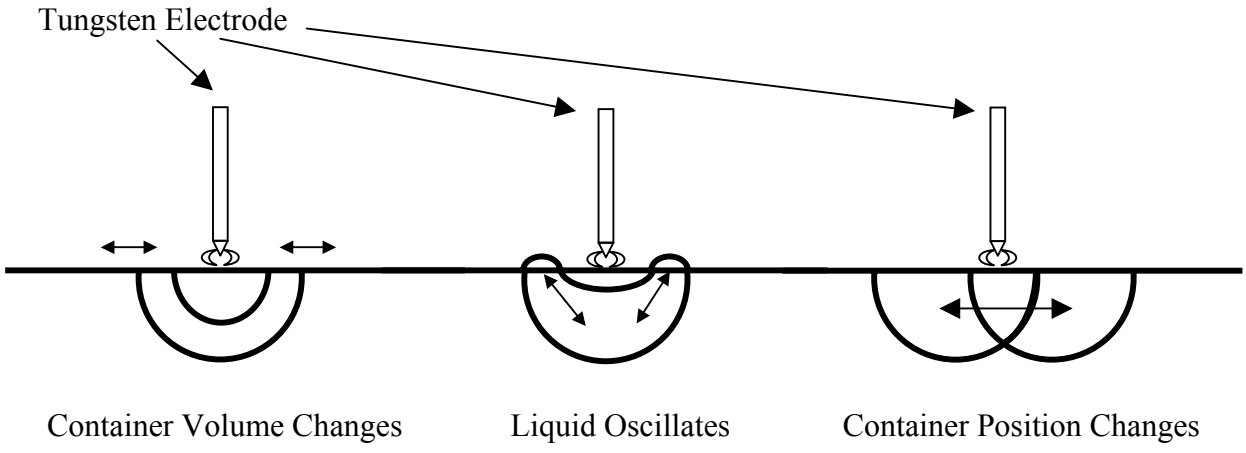

Figure 15. Schematic showing three modes of weld pool behavior that could be responsible for the observed changes in solid-liquid interface position.

arises if the container size changes (i.e. the weld pool grows and shrinks). This behavior is seen in low frequency pulsed welds. When the current pulse is applied, the solid-liquid interface retreats and the weld pool volume increases. When the current pulse is off, the solid-liquid interface advances and the weld pool volume decreases. The second mode arises if the liquid oscillates (sloshes) within the fixed container. This occurs when a natural or forced vibration causes the weld pool to oscillate. As the liquid oscillates, it alternately travels toward and away from the solid-liquid interface causing the rate of advancement of the interface to change. This mode occurs if the position of the container changes with respect to the frame of reference, in this case the tungsten electrode. Arc blow, arc wander, and variations in weld travel speed will cause this to occur.

Microstructural Features

Optical metallography of the rippled weld shows evidence of the ripple throughout the volume of the weld. Sections were made according to the diagram shown in Figure 16. Figure 17 shows a welding plane section of a rippled weld. The ripple features are visible as light arc shaped regions. In these regions the interdendritic pattern is different from the surrounding material. Figure 18 shows a transverse section of the same rippled weld. Evidence of ripples can be seen even at the bottom of the weld bead. This suggests that the rippling phenomenon is not localized at the top of the pool. Instead, the rippling event occurs throughout the volume of the melt pool.

Figure 19 shows an orientation image taken from a transverse section of a rippled weld. The edge of the weld pool, and three weld ripples can be seen. At the weld ripple, many of the image pixels are black, indicating that the electron beam system was not able to index that region. This suggests that either the grains in the weld ripple are too small to index, or that they have a different crystal structure than those elsewhere in the weld. When the indexed grains on either side of the weld ripple are compared, a change in orientation can be seen. Similar features were observed in longitudinal sections of the weld.

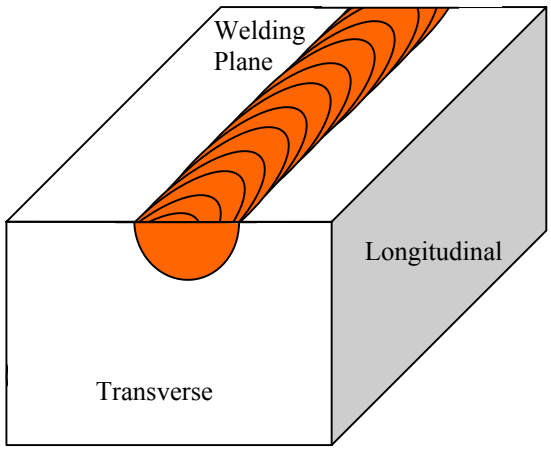

Figure 16. Schematic defining nomenclature for the orientation of metallographic sections with respect to the weld.

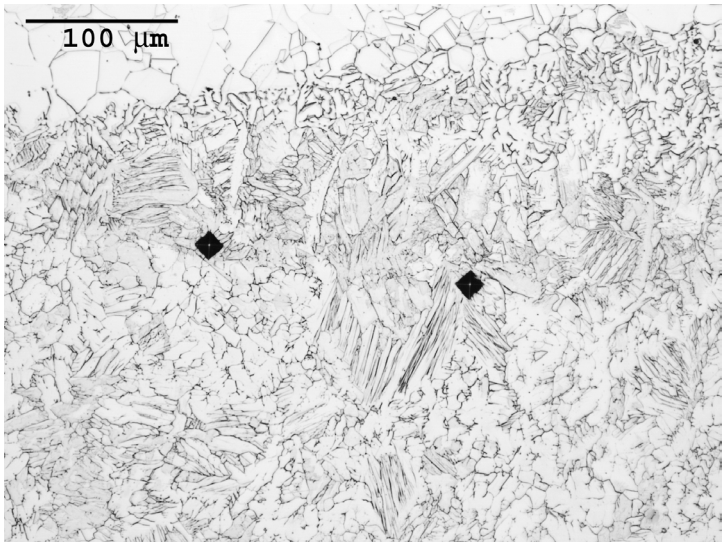

Figure 17. A welding plane section of a rippled weld showing the weld ripple feature. The indents in this image mark the ripple feature. Notice the local change in the pattern of the interdendritic material.

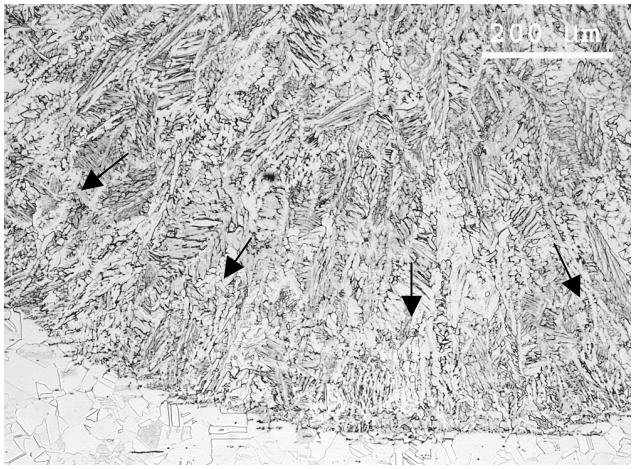

Figure 18. A transverse section of a GTA weld showing evidence of rippling in the microstructure. Arrows mark the ripple features.

Electron beam microprobe analysis showed evidence of solute redistribution associated with the weld ripple. The elements that show the most variation at the weld ripple were Cr and Ni. As might be expected, Cr and Ni levels varied in opposite directions at the ripple features. These compositional variations were subtle and as Figure 20 clearly shows, there are two sets of variations in the concentration of these elements. The fine-scale compositional variations (noted in the red and green lines) are due to solute redistribution associated with individual dendrites, while the coarse-scale compositional variations (best seen in the black, smoothed lines) are associated with the weld ripples. The composition variations are characterized by opposite changes in Cr and Ni contents, so that the Ni plot is almost perfectly antithetical to the Cr plot. The other elements, including Fe, did not show detectable changes that could be associated with the ripples.

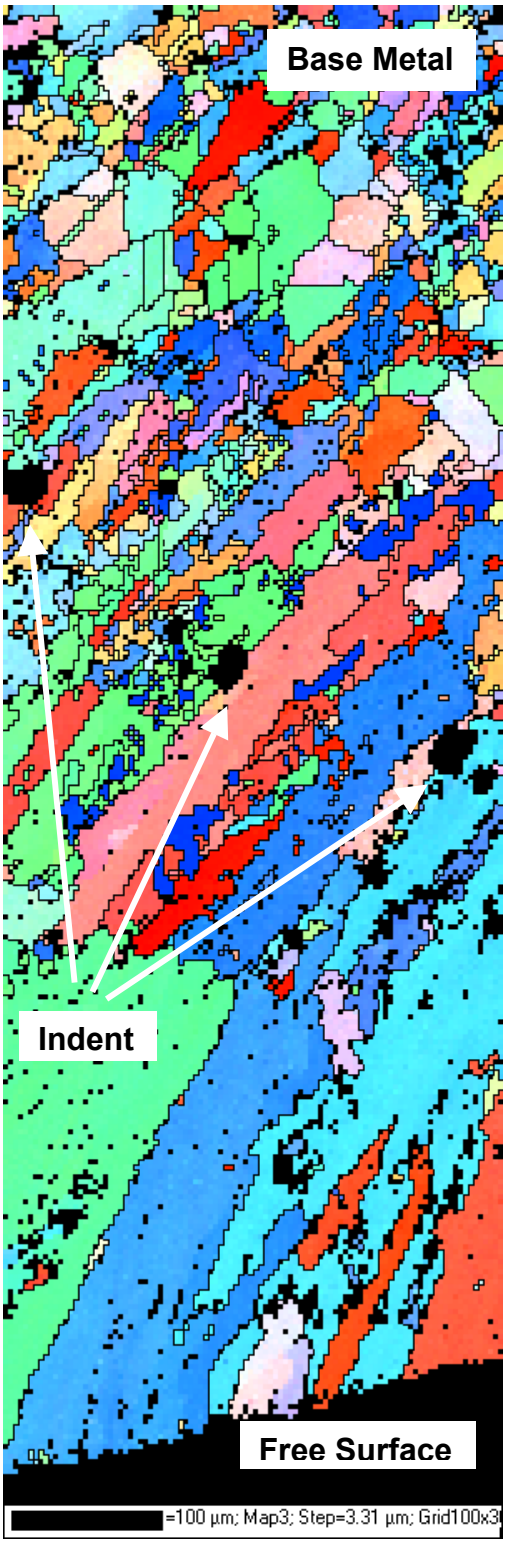

Figure 19. Orientation image showing weld ripples and changes in grain orientation in a transverse section.

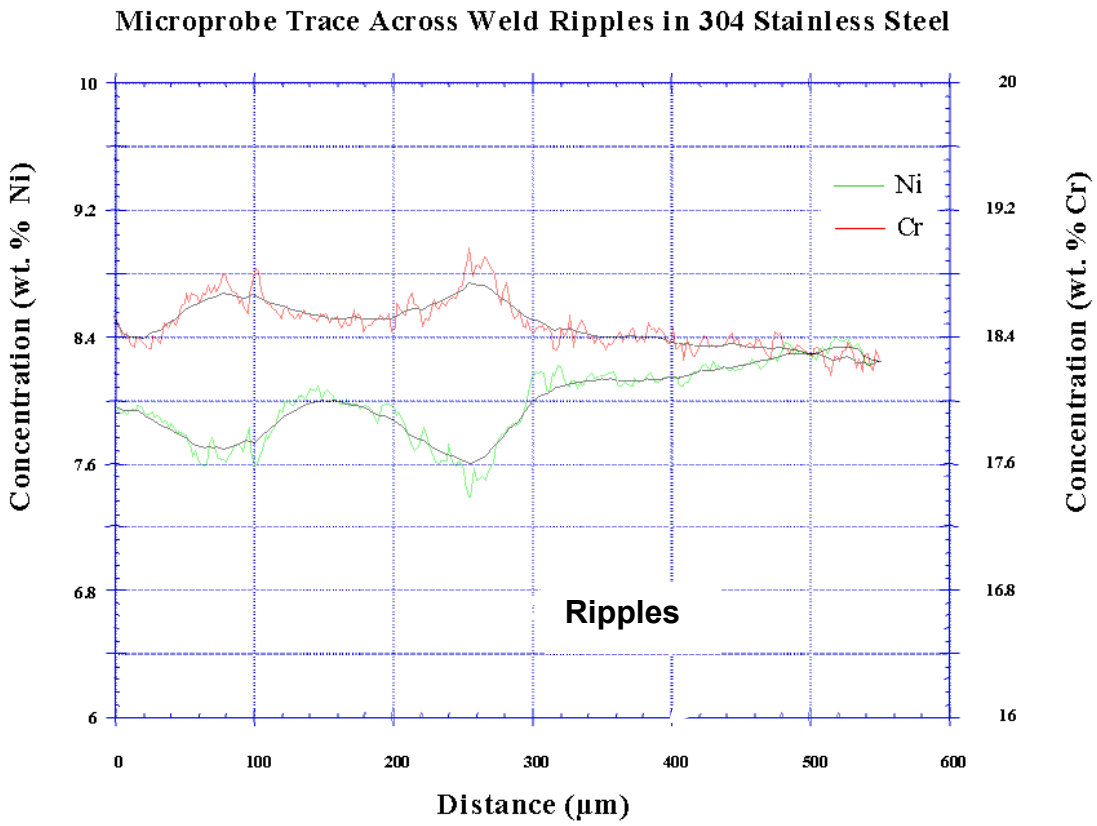

Figure 20. Variations in Cr and Ni content across 550 µm of a GTA weld showing fine scale variations due to dendrites and coarse scale variations due to weld ripples. (The red and green lines are the actual data; the black lines are the smoothed data. The scatter in the red and green lines is NOT analytical error rather it is real compositional variation due to dendrites.)

Correlation of Microstructural Features

The evidence presented above suggests that weld ripple formation is associated with changes in the solid-liquid interface velocity. Potential sources for this velocity change are described. When the velocity is negative, the previously growing dendrites are remelted. Evidence of this can be seen in the weld microstructure as a relatively abrupt change in the pattern of the interdendritic material (i.e. the growth pattern of the weld bead). During the solidification (positive velocity) portion of the rippling cycle, the interface velocity varies in a periodic way. In terms of spatial dimensions, the period of the velocity oscillation is approximately 150µm. This period correlates with an observed oscillatory change in composition. As shown below, the composition change is expected with changes in solidification velocity.

It is well known that solute partitioning at the solid-liquid interface in a solidifying metal is a function of solidification velocity. The antithetical rejection of Cr and Ni can be explained

as follows. In the simple case of planar solidification, solute pileup at the solid-liquid interface can be described by (Kurz and Fisher 1992):

$$C_0 = C_0 + \Delta C_0 \exp\left(-\frac{V_z}{D}\right) \quad (1)$$

Where:

C_l = solute concentration in the liquid
C_0 = initial alloy concentration
V = rate of interface movement
z = coordinate perpendicular to a planar solid/liquid interface
D = diffusion coefficient in the liquid
ΔC_0 = concentration difference between the liquidus and the solidus at the solidus temperature of the alloy, typically $\Delta C_0 = C_0 \frac{(1-k)}{k}$, where k is the partition coefficient

However, ΔC_0 can also be described by:

$$\Delta C_0 = \frac{\Delta T_0}{m} \quad (2)$$

Where:

ΔT_0 = liquidus-solidus temperature range at C_0
m = liquidus slope

Combining equations (1) and (2):

$$C_l = C_0 + \frac{\Delta T_0}{m} \exp\left(-\frac{V_z}{D}\right) \quad (3)$$

Elmer examined the Fe-Ni-Cr phase diagram near the composition of 304 stainless steel and showed that the slope of the liquidus surface for changing Cr and Ni concentrations are different. In fact for both primary ferrite and primary austenitite solidification, they are opposite in sign (Elmer 1988). Knowing this, equation (3) explains the antithetical rejection of Cr and Ni that was observed. C_0 and ΔT_0 are finite and constant. The exponential term in equation (3) is positive for any velocity. Thus, if the slope of the liquidus (m) is positive, then C_l will always relate directly to V. If the slope of the liquidus is negative, C_l will always relate inversely to V. Since the slopes of the Cr and Ni liquidus lines in 304 stainless steel are always opposite in sign, changes in Cr and Ni concentration during solidification should be antithetical. This behavior is well known in relation to microsegregation (i.e. at the scale of the solidification cell), as well as in relation to macrosegregation (i.e. in castings). As shown here, there is an additional scale of solute redistribution in rippling welds that is related to oscillatory changes in the solid-liquid interface velocity.

This presents the following question: Is the formation of the weld ripple the result of oscillation of the weld pool or is it the result of a change in the solid-liquid interface velocity? The answer is both, since the two are effectively the same. Oscillation of the liquid weld pool is a velocity change in the solid-liquid interface frame of reference. This conclusion has some interesting implications: First it suggests that cyclic mechanical motion of the liquid pool will

result in recognizable changes in the microstructure of the weld metal. It also suggests that the effect of bulk pool motion has a different impact on the weld microstructure than fluid convection, or Maringoni flow. Lastly, it suggests that if mechanical motion of the liquid pool is responsible for the microstructure modification associated with weld ripples, then it should be possible to deliberately modify weld microstructure by inducing mechanical motion of the weld pool. Of course, this has long been qualitative recognized in a practical sense, and has been used as a rationale for applying electrical pulsing, magnetic arc oscillation, or vibratory means for weld modification. However, the present work provides a quantitative means for assessing the basic mechanisms for weld microstructure control using these approaches.

Computer Model Validation Using High-Speed, High-Magnification Video Measurements of Solidification Velocities

Introduction

Small diameter (~1mm) laser spot welds are commonly used to permanently fasten small components after assembly. Precise fit-up and low distortion are required in order to maintain the dimensional integrity of the welded assembly (Mazumder 1982). Finite element models of the laser spot welding process are being developed so that more effective welds can be made. Validation and verification is an integral part of this modeling effort. In this case, visualization experiments were used as a validation tool. A Nd-Yag laser was characterized and used to make a series of small diameter laser spot welds. These welds were filmed using a high-speed camera. The diameter of the liquid pool was measured from the video images. This information was used to generate graphs of pool diameter versus time and to calculate the solidification velocity of the welds. Pool diameter versus time is directly predicted by the computer model and is dependent on the thermal boundary conditions. The experimental information is used to validate the model and the prediction of the formation of the weld pool. This section will describe the model and the experimental procedures used to validate it. Predicted and experimental data will be compared and discussed.

Model Description

The finite element code (Shunk et.al 1998) modified for use in this investigation uses an arbitrary Lagrangian / Eulerian finite element method. This code employs a unique fully-coupled, pseudo-solid mesh motion scheme to track the solid and liquid phase regions as defined in Figure 21. Over 2000 4-node quadrilateral elements are used in the generation of the mesh for the axisymmetric, transient welding simulations. The time dependent interface between the weld pool and solid regions is defined by the melting temperature isotherm. Solutions are obtained

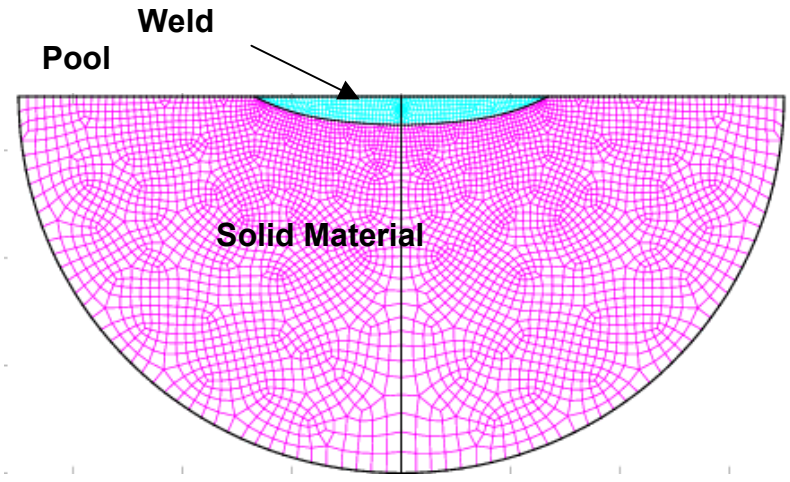

Figure 21. Finite element mesh used in calculations.

using a full-Newton coupled algorithm for the mass, momentum, energy, and mesh equations. The boundary conditions for the momentum equation on the weld pool free surface consists of a zero shear stress condition and a balance of the pressure and viscous stress by the surface tension acting on the surface. The free surface boundary conditions remain active during these simulations even though no keyhole formation was simulated during this effort. Boundary conditions for the energy equation are defined in Figure 22. Both convective and radiative heat losses are included in the thermal boundary condition for the surface of the test piece. Latent heat release at the melting front is included as a heat flux term on the liquid interface between the weld pool and solid material.

The laser heat flux distribution on the material surface varies temporally and spatially. A Gaussian distribution of the laser heat flux is used that assumes the heat flux to vary only along the laser beam radius. The temporal variation of the laser is currently handled by assuming that the laser heat flux remains constant during the laser pulse, and then decreases linearly after termination.

A series of four solutions were obtained for each laser spot weld simulation. Each solution is a continuation of the previous solution, and represents a specific physical regime in the development of a weld pool. The first is the conduction-only solution where only the energy equation is needed to generate a solution. Once the liquidus temperature is reached in the weld pool, the mass and momentum equations are included to simulate the development of the liquid region of the pool. Next, the mesh motion equations (Sackinger et. al. 1996) are added when the weld pool has reached a sufficient size to include the tracking of the melting front. The final solution is initiated after the laser pulse has been terminated to simulate the cool down process. If excessive mesh distortion becomes an issue to the accuracy of the predictions, a remeshing and solution remapping step was performed to recondition the solution and achieve greater accuracy.

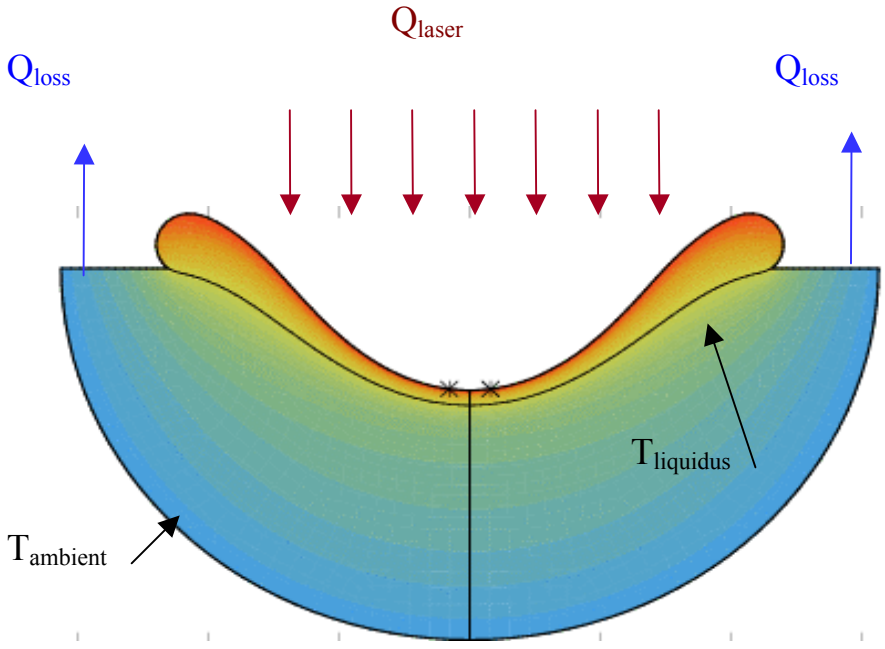

Figure 22. Thermal boundary conditions used in finite element model.

Experimental Procedures

Laser Welding

All of the laser spot welds were made using a 1500 W Rofin Sinar® continuous wave Nd-Yag laser model CW 015HQ. This continuous wave laser was operated in a pulsed mode in order to simulate a pulsed laser weld. A pulsed output is created by varying the flash lamp current. A background or simmer current level is set, a pulse current level is set, and a pulse duration is set. When the laser is triggered, the flash lamps are energized in accordance with these parameters, creating a moderate duration laser pulse.

Beam Characterization

The laser beam was characterized at a number of different nominal powers using an Optical Engineering® P-1000Y power probe and a 4 inch diameter Labsphere® integrating sphere. The power probe is a calorimeter-type power meter. It is operated by exposing the absorbing mass of the power probe to the laser beam for a specified period of time. The average power absorbed during the exposure is displayed on a calibrated analogue scale. This device was used to calibrate the nominal power settings of the laser. An integrating sphere is a hollow, water-cooled sphere with a reflective coating on its interior. A laser beam enters the integrating sphere through an aperture and is reflected within the sphere. A small CCD camera in the wall of the sphere samples the light intensity and provides a voltage output. This output is directly related to the power of the laser beam. The integrating sphere provides excellent temporal resolution and was used to characterize the shape of the laser pulse.

Visualization Scheme

The laser spot weld was filmed using a Speed Vision imager equipped with a Navitar lens. The camera and lens were placed above a turning mirror. This positioning of the lens allowed the laser spot weld to be viewed from directly above (along the axis of the laser beam). All of the laser spot welds were filmed at 2000 frames per second. An accurate scale was filmed to give a length calibration.

Results and Discussion

Beam Characterization

The thermal characterization of the laser beam is shown in Figure 23. This allows nominal power settings of the laser to be interpreted as a specific energy level. The integrating sphere was then used to measure the laser beam at the same nominal power settings, Figure 24.

This data was used to correlate the voltage reading of the integrating sphere with the thermal measurement from the power probe, Figure 25. After these measurements were made, laser pulses identical to those used for welding were measured using the integrating sphere. These pulses are shown in Figure 26. Note that the pulses have a peak and a background plateau.

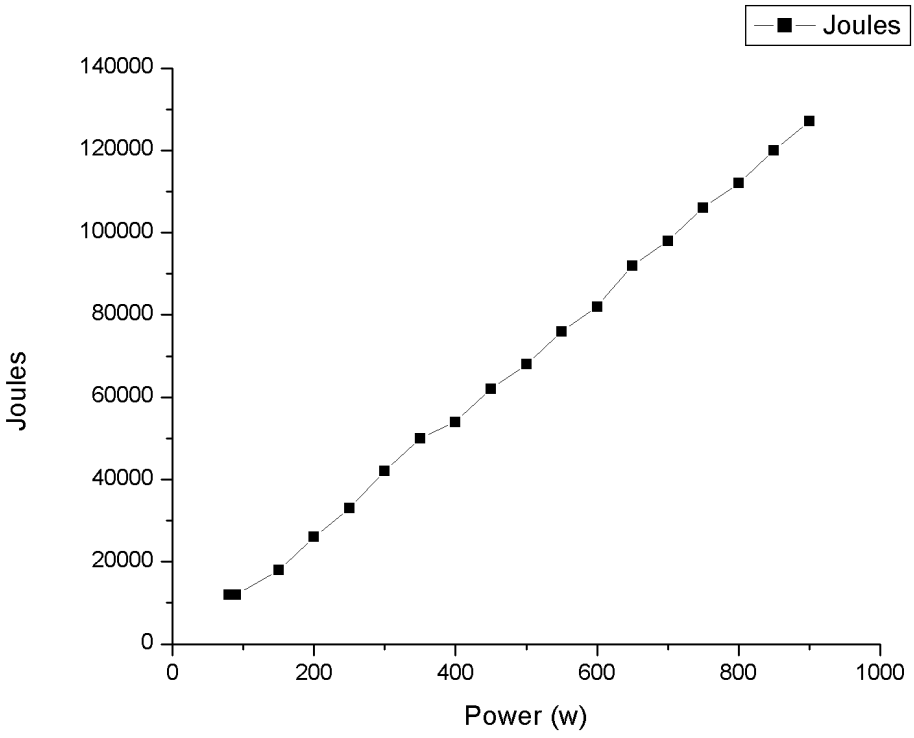

Figure 23. The relationship between nominal laser power in watts and beam energy in Joules is shown in this power meter data.

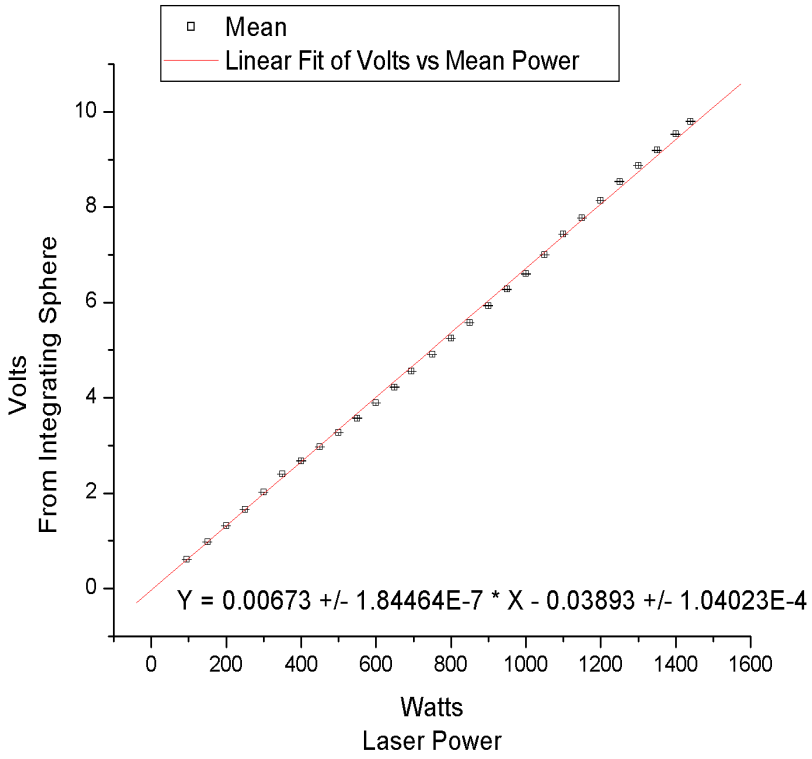

Figure 24. Voltage measurements from the integrating sphere at a number of different nominal laser powers.

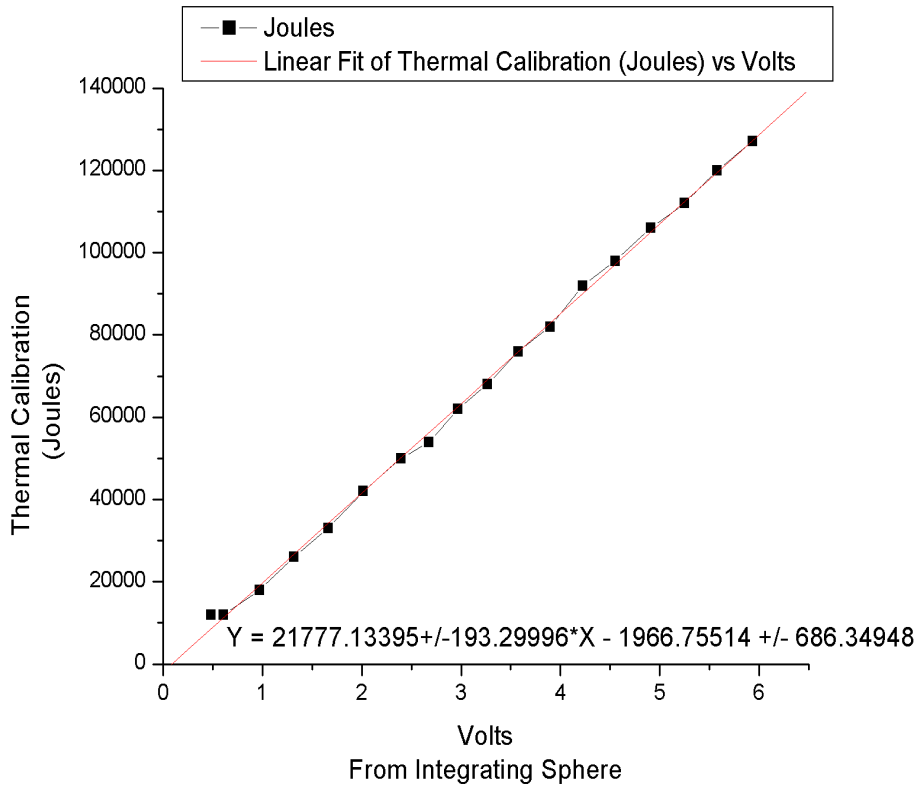

Figure 25. Combination of Figures 3 & 4 shows the relationship between integrating sphere volts and the power meter energy measurements.

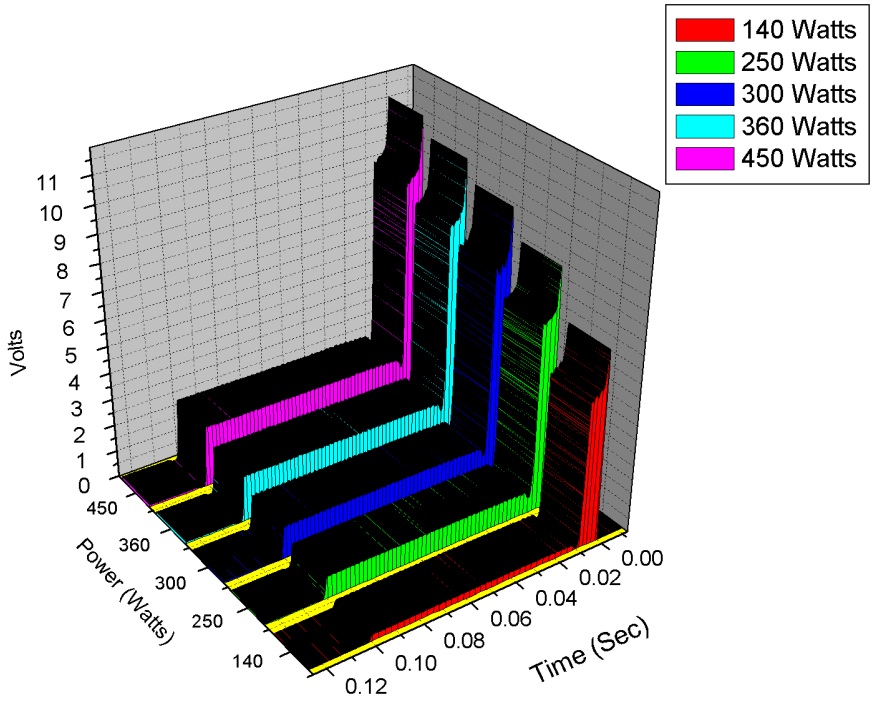

Figure 26. The temporal energy distribution of the laser pulse is shown in these integrating sphere measurements.

This occurred because the laser creates a pulse by varying the flash lamp current from a background level to a pulse level.

Figure 27 shows a still image from a video of a laser spot weld. The liquid pool diameter was measured from images like this using image analysis software.

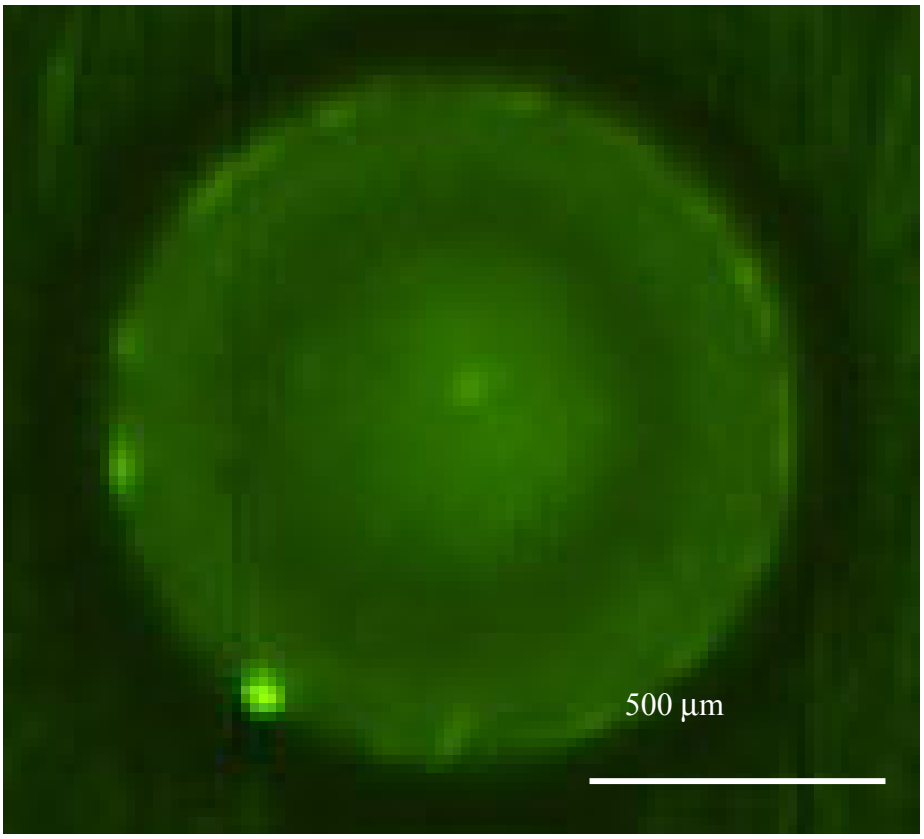

Figure 27. A still image of a laser spot weld in 304 stainless steel.

Figure 28 shows the measured liquid pool diameters for a series of welds at four different nominal laser powers. The 250 and 300 Watt welds show liquid pool diameter data for only the initial part of the laser pulse because the plateau in the laser pulse did not cause any measurable remelting. Remelting was observed in the higher power welds (360 and 450 Watts) and is reflected in the measurements of liquid pool diameter. The remelting was a result of the laser power decreasing to the background plateau level rather than shutting completely off after the laser pulse was completed as shown in Figure 26. Figure 29 shows a cross section of a 360 Watt weld, evidence of remelting can be clearly seen.

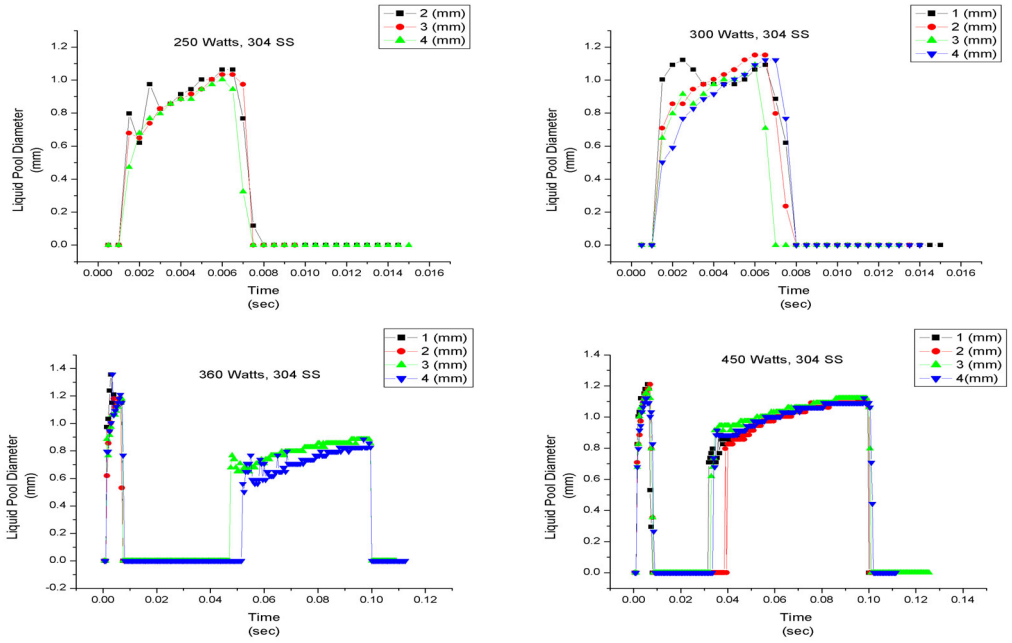

Figure 28. Liquid pool diameter versus time for four different nominal laser powers.

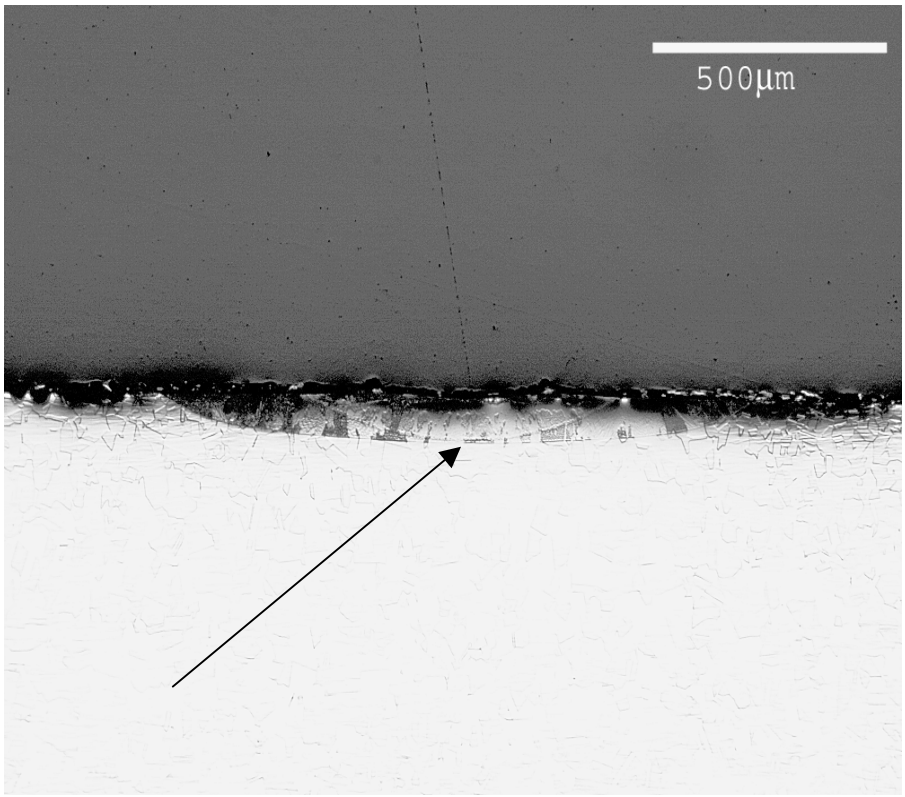

Figure 29. Cross section of a 360 watt laser spot weld. The arrow points to the boundary of the remelted region.

Comparison of Predictions and Experiment

Simulations were performed for the 450, 360, 300, and the 250 Watt welds with the results shown in Figures 30 through 33. Overall the model results matched well with the experimental results for the maximum pool diameters and the pool depths. However, discrepancies of predicted pool diameters and the measured pool diameters did occur at the beginning and termination of the laser pulse especially at the lower laser powers.

The 450 Watt weld showed the best matching of experimental and simulation results. Figure 30 contains the 450 Watt comparisons of the pool diameter versus time. The pool diameter predictions matched well with the experimental measurements except at the beginning of the laser pulse. Figure 31 shows the comparison of experiment and simulation for the weld cross-section. The overall shape of the simulated pool matches well with experiment, but the maximum depth is ~20% shallower than the experimental result. Both results in Figures 30 and 31 indicate that the energy balance is an area of improvement for both the experiment and the finite element model.

Figures 32 and 33 show the results for the 300 Watt weld. Comparison of the pool diameters as shown in Figure 32, show that the predicted pool diameters are consistently smaller than experiment during the entire laser weld, especially at the beginning of the weld. Also, the pool cross-section is again shallower for the simulation when compared to experiment as shown in Figure 33.

While the results of experiment and simulation are quite promising, the differences in the simulation and experimental results in Figures 30 thru 33 indicate the need for further refinement in both the experiment and the finite element model.

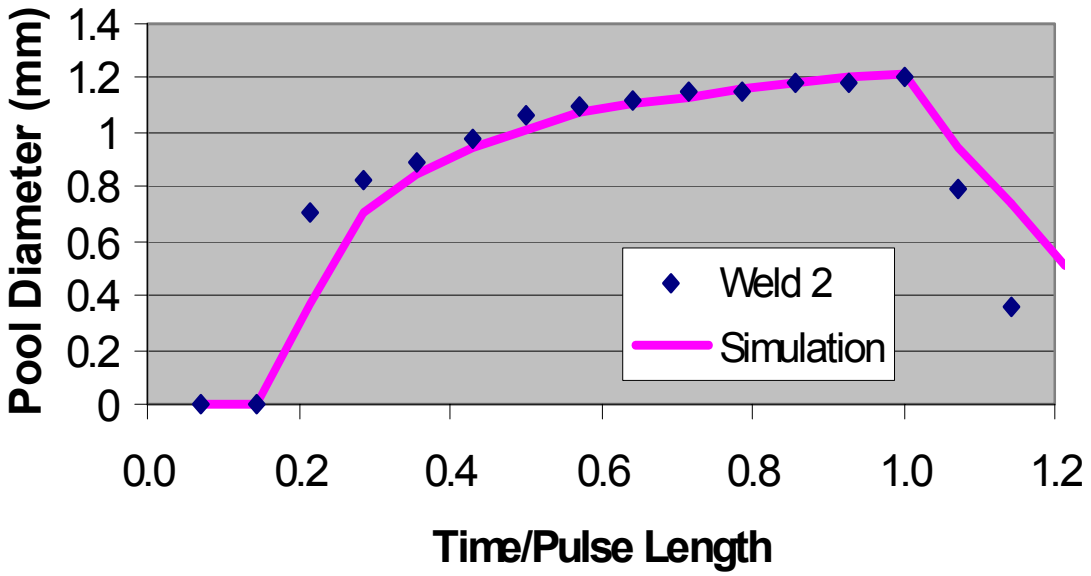

Figure 30. Comparison of experimental and simulated pool diameters versus time for 450 watt weld.

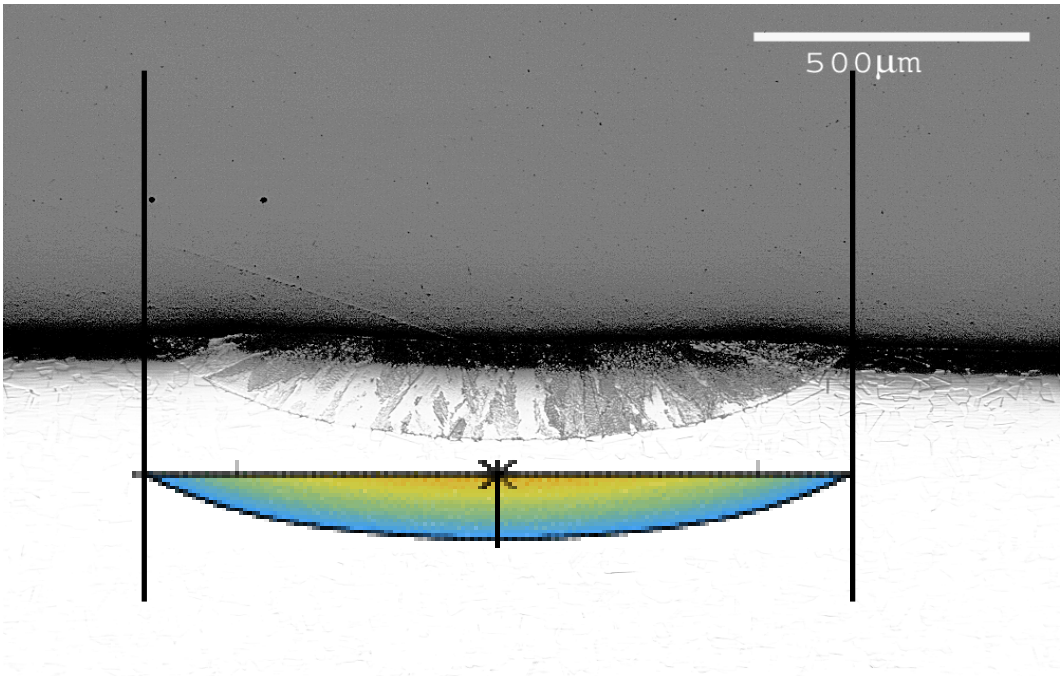

Figure 31. Comparison of experimental and simulated pool cross-section for 450 watt weld.

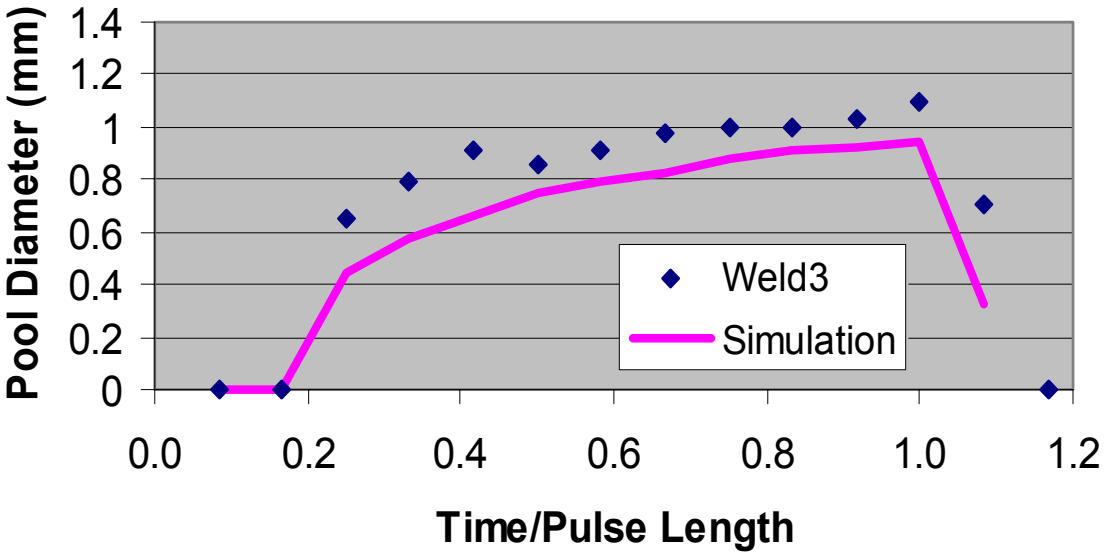

Figure 32. Comparison of experimental and simulated pool diameters versus time for 300 watt weld.

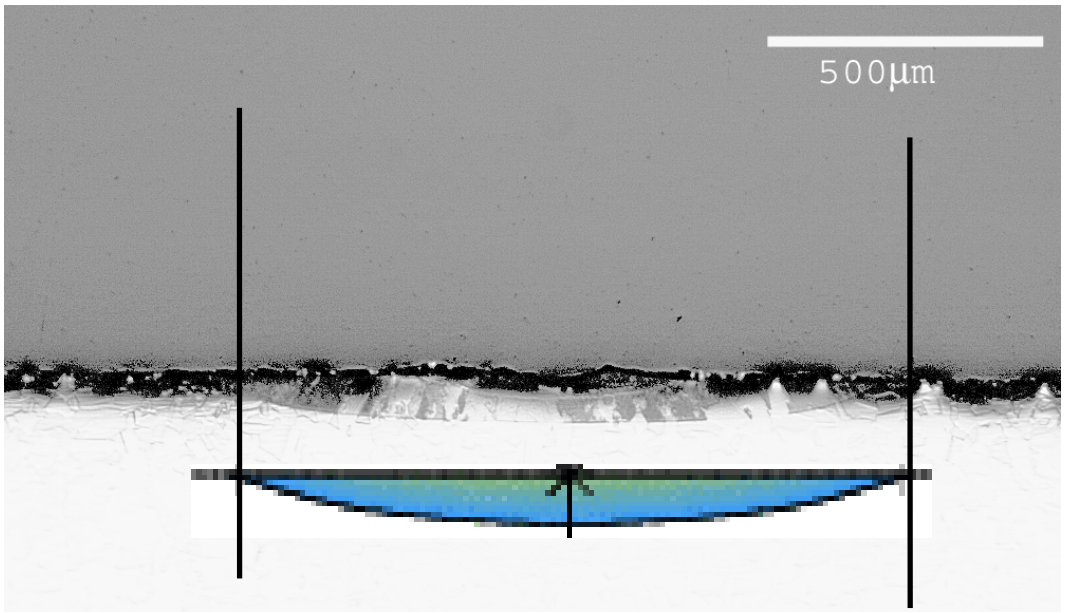

Figure 33. Comparison of experimental and simulated pool cross-section for 300 watt weld.

An obvious area of improvement for the model is the definition of the laser heat flux. The temporal behavior of the laser shown in Figure 26 shows a large spike at the beginning of the laser pulse that could initiate boiling for a very brief period of time at the beginning of the weld. As discussed previously, the laser heat flux distribution currently used in the model assumes a constant laser heat flux during the pulse. Accounting for the spike in heat flux at the beginning of the weld increased the heat transfer rate at the surface of the pool and explained the difference observed between the predicted and measured pool diameters and pool depths. The radial distribution of the laser heat flux also needs to be experimentally measured to verify the Gaussian distribution assumed in the model.

The thermal boundary conditions used in the model also need validation. Effective laser absorptivity levels used in this effort are typical of those used by other authors (Fuerschbach and MacCallum 1995; Ki, Mohanty et al. 2001), but should be experimentally verified. Several simplifying assumptions for non-keyholeing processes were also incorporated in this model. Evaporation phenomena were assumed negligible for welds with no keyhole formation. This assumption should also be experimentally verified for future efforts.

The material properties used in the calculations are typical values for 304 stainless steel. It is possible that the properties of the 304 samples used for the experimental welds are different from these values. Absorptivity, latent heat of melting and thermal conductivity of the actual sample material should be measured and used as model inputs. This can only improve the accuracy of the predictions.

Measurement error can always occur even in well-planned experiments. While the most likely source of the differences between model and experiment is the unexpected large spike in the laser pulse, it is possible that other measurement errors do exist. The temporal resolution of the integrating sphere may not be fast enough to fully capture the initial spike in the laser pulse. Changes in lighting conditions could make the liquid pool diameter appear larger or smaller than its true measurement. The thermal calibration could be in error; this would result in an incorrect energy input for the model. As this model and experimental comparison is further refined, all these potential sources of error will be considered.

Summary of Visualization Studies

The solid-liquid interface in a variety of welds have been successfully filmed at high magnification and high frame rate. A tremendous amount of information about the motion and evolution of the solid-liquid interface can be harvested from these videos. This technique is an excellent way to directly measure dynamic processes occurring in a solidifying weld. Unlike experimental schemes based on confocal scanning laser microscopy or transparent polymers; high-speed, high-magnification video can provide information about solid-liquid interface motion in engineering materials in actual welding environments. Information (like primary and secondary dendrite arm spacings) gathered at the surface of the weld pool can be associated with features deeper in the pool. This should be done with appropriate caution. Nevertheless, measurements of the solid-liquid interface made using this technique are useful for fundamental solidification science, and computer model validation and verification.

Weld rippling phenomenon was investigated using high-speed, high-magnification video microscopy. The solid-liquid interface velocity associated with the weld ripple formation was measured using video images. It is clear that the solid-liquid interface velocity changes during the ripple formation. It also appears that the instantaneous growth direction at the solid-liquid interface changes during the ripple event. Optical metallography shows that the ripple feature is present throughout the weld bead. Electron microprobe analysis confirmed that compositional variations are associated with weld ripples. Cr and Ni were the elements that showed the most variation, with changes in Ni content being antithetical to Cr. This evidence suggests that weld ripples are associated with significant changes in the solidification front velocity. These velocity changes produce specific changes in weld microstructure.

Time resolved measurements of the liquid pool diameter in small laser spot welds were made using high speed imaging techniques. This data was directly compared to predicted values of liquid pool diameter generated from a physics based model of a laser spot welds. The comparison was excellent at high laser powers. The experimental data matched the predicted values well over the duration of the spot weld. At lower laser powers the comparison was not as good. The model predicted the final diameter of the laser spot weld correctly, but the predicted diameter did not match the measured diameter over the entire duration of the weld. This suggests that additional physics may need to be incorporated in the model. The primary improvements to the model are a better definition of the laser heat flux and verification of the material properties used in this investigation. The results also suggest that measurement error may exist for low laser powers.

The experimental techniques used to measure the laser spot welds in this investigation are simple, straightforward, and provide a tremendous amount of information. Their real value is in the ability to capture the dynamic phenomena associated with the laser spot weld. Without this dynamic information the inconsistency at low power would not have been detected.

References for Visualization Studies

Aendenroomer, A. J. R. and G. denOuden, 1998, *Welding Journal Research Supplement,* vol. 77 (5), pp. s181-s187.

Andersen, K., G. E. Cook, et al., 1997, *IEEE Transactions On Industry Applications* **33**(2), pp. 464-471.

Babb, M., 1995, *Control Engineering*, July.

Brooks, J. A., N. Y. C. Yang, et al., 1993, *Int. Trends Weld. Sci. Technol., Proc. 3rd Int. Conf. Trends Weld. Res.,* pp. 173-80.

D'annessa, A. T., 1970, *Welding Journal Research Supplement,* vol. 49(2), pp. 41s-45s.

DuPont, J. N., C. V. Robino, et al., 1998, *Acta Mater,* vol. 46(13), pp. 4781-4790.

Ecer, G. M., A. Gokhale, et al., 1980, *Journal of Metals,* vol. 32(8), pp. 80-80.

Elmer, J. W., 1988, PhD Thesis, *Department of Materials Science and Engineering, MIT* Cambridge, p. 388.

Elmer, J. W., S. M. Allen, et al., 1989, *Metallurgical Transactions A,* vol. 20A(October), pp. 2117-2131.

Fuerschbach, P. W. and D. O. MacCallum, 1995, ICALEO.

Garland, J. G. and G. J. Davies, 1970, *Metal Construction and British Welding Journa,l* May, pp. 171-175.

Glicksman, M. E., M. B. Koss, et al., 1995, " *ISIJ International,* vol. 35(6), pp. 604-610.

Glicksman, M. E., M. B. Koss, et al., 1995, *Advances in Space Research,* vol. 16(7), pp. 181-184.

Glicksman, M. E., M. B. Koss, et al., 1996, *Solidification and Gravity,* vol. 215, pp. 179-189.

Hall, A. C., C. V. Robino, et al., 2001, *11th International Conference on Computer Technology in Welding*, American Welding Society, Columbus, OH.

Hogarth, S., 1999, *Manufacturing Engineering,* vol. 122, pp. 102-104.

Huang, W., Y. Inatomi, et al., 1997, *Journal of Crystal Growth,* vol. 182, pp. 212-218.

Ki, H., P. S. Mohanty, et al., 2001, *J. Phys. D: Appl. Phys.,* vol. 34, pp. 364-372.

Kotecki, D. J., D. L. Cheever, et al., 1972, *Welding Journal Research Supplement,* August, pp. 386s-391s.

Kurz, W. and D. J. Fisher, 1992, Trans Tech Publications.

Mazumder, J., 1982), *Journal of Metals,* vol. 34(7), pp. 16-24.

Mazumder, J., 1991, *Optical Engineering,* vol. 30(8), pp. 1208-1219.

Morvan, D. and P. Bournot, 1995, *Proceedings of SPIE The International Society for Optical Engineering,* vol. 2502, pp. 643-649.

Morvan, D. and P. Bournot, 1996, *International Journal of Numerical Methods for Heat and Fluid Flow*, vol. 6, pp. 13-20.

Nemchinsky, V. A., 1997, *Int. J. heat Mass Transfer,* vol. 40(4), pp. 881-891.

Orrling, C., Y. Fang, et al., 2001, *Journal of Metals-electronic,* vol. 53, pp. 1-8.

Orrling, C., Y. Fang, et al., 1999, *Journal of Metals-electronic,* vol 51(7).

Postacioglu, N., P. Kapadia, et al., 1991, *Journal of Physics D-Applied Physics,* vol. 24(8), pp. 1288-1292.

Sackinger, P. A., Schunk, P.R., and Rao, R.R., 1996, *J. Comp. Physics*, vol. 125, pp. 83-103.

Schunk, P.R., Sackinger, P.A., Rao, R.R., Chen, K.S., Cairncross, R.A., Baer, T.A., Labreche, D.A., 1998, Sandia Report, SAND97-2404, Sandia National Laboratories, Albuquerque, NM.

Schwartz, A. J., K. M, et al., Eds., 2000, *Electron Backscatter Diffraction in Materials Science,* New York, Kluwer Academic/Plenum Publishers.

Wei, P. S., C. Y. Chang, et al., 1996, *Journal of Heat Transfer-Transactions of the ASME, vol.* 118(4), pp. 960-969.

Zuech, N., 2000, *Advanced Imaging*, vol. 15. p. 3.

Solidification Microstructures in Fe-Cr-Ni Alloys

Introduction

The crystallographic orientation relationship (OR) between two phases with different crystal structure is an important parameter affecting microstructure-property relationships in such processes as precipitation from solid solution, martensitic transformation, epitaxial growth, and solidification. An OR between two phases is often found in solidification microstructures where the relationship is established either during solidification or during subsequent solid state transformation on cooling. For example, the weld or cast microstructures of austenitic stainless steels frequently contain ~2-10 volume percent delta-ferrite (δ) in the austenite (γ) matrix. Both alloy composition and solidification/cooling conditions dictate whether or not an OR is established between delta-ferrite and austenite in the resultant two-phase microstructure. Although extensive studies have been published on the solidification and microstructural evolution in austenitic stainless steel welds and castings (Brooks and Thompson 1991, Brooks *et. al.* 1981, Brooks *et. al.* 1983, Brooks *et. al.* 1992, Brooks *et. al.* 1984, Inoue *et. al.* 2000, Inoue *et. al.* 1997, Inoue *et. al.* 1998, Suutala *et. al.* 1979a, Suutala *et. al.* 1979b, Suutala *et. al.* 1980) it is not always straightforward to determine when the two phases were formed, or if an OR existed between delta-ferrite and austenite, when it was established. This is due in part to the complex nature and wide range of ferrite morphologies that can exist even within a single solidification structure (David 1981).

The structure of delta-ferrite is body-centered-cubic (bcc) and that of austenite is face-centered-cubic (fcc). Historically, a small number (five) of ORs has been reported to exist between bcc and fcc lattices. The three best known are the Bain (Bain 1924), the Kurdjumov and Sachs (K-S) (Kurdjumov and Sachs 1930), and the Nishiyama and Wasserman (N-W) (Nishiyama 1934, Wasserman 1933) ORs. The Greninger and Triano (G-T) (Greninger and Triano 1949) and the Pitsch (Pitsch 1959) ORs are less well known. It is common practice to describe an OR by a set of planes that are parallel in the two lattices and a set of directions within those planes that are parallel. This information is given in Table I for the five known bcc-fcc ORs.

The Bain OR was proposed first in 1924 (Bain 1924) to explain the martensite (martensite, with small tetragonal distortion, is found experimentally to obey the same ORs as bcc lattices and is grouped with the bcc system in this description) transformation in carbon steels in terms of a simple set of orthogonal strains that would transform the austenite lattice directly to the martensite lattice. It is now well known that the Bain distortion alone is not sufficient to describe the martensitic transformation in carbon steels (Barrett and Massalski 1966) and the Bain OR is not observed for martensite in these alloys. The Bain OR has been observed for ordered Fe_3Pt martensites and Fe_3Al-C martensite in high-aluminum steel (Shimizu and Nishiyama 1972). It has not been reported for ferrite-austenite microstructures in steels, however. The K-S and N-W ORs are the most frequently reported relationships for bcc-fcc systems including martensites in steels, and they are the only ones that have been reported for ferrite-austenite microstructures. These two relationships differ from each other by a small relative rotation of 5.26°. The G-T OR was reported for martensite in steel containing 0.8%C and 22% Ni. It lies approximately midway between K-S and N-W ORs, being rotated 2.5° from

Table I. Summary of Known bcc-fcc Orientation Relationships.

Name	Orientation Relationship	Close-packed Components Parallel	Minimum Angle between $<110>_{fcc}$ and $<110>_{bcc}$
Bain	$(010)_{fcc}//(010)_{bcc}$, $[001]_{fcc}//[101]_{bcc}$ and $[100]_{fcc}//[10\text{-}1]_{bcc}$ $[101]_{fcc}//[100]_{bcc}$ $[\text{-}101]_{fcc}//[001]_{bcc}$	none	45°
Kurdjumov-Sachs (K-S)	$(111)_{fcc}//(110)_{bcc}$, $[\text{-}110]_{fcc}//[\text{-}111]_{bcc}$ and $[11\text{-}2]_{fcc}//[\text{-}11\text{-}2]_{bcc}$	c.p.-planes c.p.- directions	24.74°
Nishiyama-Wassermann (N-W)	$(111)_{fcc}//(110)_{bcc}$, $[\text{-}101]_{fcc}//[001]_{bcc}$ and $[\text{-}12\text{-}1]_{fcc}//[\text{-}110]_{bcc}$	c.p.-planes	25.02°
Greninger-Triano (G-T)	$(111)_{fcc}$~1° from$(110)_{bcc}$, $<112>_{fcc}$~2° from$[1\text{-}10]_{bcc}$	~c.p.-planes	~25°
Pitsch	$(001)_{fcc}//(101)_{bcc}$, $[\text{-}110]_{fcc}//[\text{-}111]_{bcc}$ and $[110]_{fcc}//[12\text{-}1]_{bcc}$	c.p.-directions	25.02°

the N-W OR. The Pitsch OR (Pitsch 1959) was observed for martensite formed in thin foils of an iron-nitrogen alloy, not subject to bulk lattice constraints as are martensites that form in bulk with the K-S or N-W OR. Neither the G-T nor Pitsch OR has been reported for ferrite-austenite microstructures. In summary, only five different ORs have been reported previously for bcc-fcc systems. Of these, the K-S and N-W ORs are the most frequently encountered and are the only ones that have been reported for ferrite-austenite microstructures.

While investigating solidification microstructures in 304L stainless steel fabricated by laser-engineered-net-shaping (LENS) (Griffith *et. al.* 1996) and gas tungsten arc (GTA) welds in 309S stainless steel and a ternary Fe-Cr-Ni alloy, we observed a new OR between delta-ferrite and austenite within some grains. Evidence for this new OR was obtained from selected-area electron diffraction (SAED) patterns in transmission electron microscopy (TEM). This new OR has not been previously reported for bcc-fcc lattices, i.e. it is not one of the five known ORs listed in Table I. We report here experimental evidence for the new OR and experimental conditions for which we have observed it.

Experimental

The new OR was observed in solidification microstructures of two austenitic stainless steels, types 304L and 309S, and a ternary Fe-Cr-Ni alloy. Heat compositions for the three alloys are given in Table II. The solidification structures were produced by LENS-fabrication of the 304L alloy, and by GTA welding of the 309S and Fe-Cr-Ni alloys. In the LENS process, three-dimensional engineering components are fabricated using lasers to melt fine metal particles. In LENS-fabrication of the 304L alloy, metal particles were fed into a molten pool formed by a 1 kW continuous YAG laser. The sample was fabricated into a block 76 mm long and 9.5 mm wide using alternating layers, each comprised of overlapping passes with ~0.4 mm spacing. The passes were made with a laser power of 700 watts, travel speed of 40 mm/s, and powder feed rate of 0.33 gm/s. The alternating layers were deposited with a 90° rotation between layers. The height of each layer was approximately 0.25 mm. The 309S alloy in the form of 0.25 mm sheet was GTA welded at 10.6 mm/s with 17 amps, 15 volts, and argon shielding. The ternary Fe-Cr-Ni alloy in the form of 9.5 mm plate was also GTA welded, but weld parameters were unavailable.

Table II. Alloy compositions, wt.%.

Alloy/Process	Heat	Cr	Ni	Mn	Si	C	N	P+S	Fe
304L/LENS	2	19.7	11.9	1.74	0.59	0.04	-	-	bal.
309S/GTA weld	4A	25.1	14.0	1.56	0.73	0.05	~.02	0.92	bal.
Fe-Cr-Ni/GTA weld	8342	18.67	11.34	-	.008	.009	.003	-	bal.

Thin foils for TEM analysis were prepared by electropolishing in a solution of 5% perchloric acid in methanol at –25 °C with an applied potential of 18 V. Some foils were Ar ion-milled following electropolishing to increase the amount of thin area for observation, or to thin a specific grain or ferrite particle within a grain sufficiently for electron diffraction analysis. TEM analyses were performed on a PHILIPS-CM30 TEM at 300 kV and a JEOL-2000FX TEM at 200 kV using standard imaging and SAED techniques. Computed SAED patterns were generated using Desktop Microscopist (Desktop Microscopist is a software program copywrited and licensed by Virtual Laboratories. for comparison with experimental SAED patterns).

Results

304L LENS Block

We first observed ferrite with the new OR within several austenite grains in the microstructure of the 304L LENS-fabricated block. Figure 34(a) shows the optical microstructure of this block at low magnification where the individual passes within different layers are clearly visible. Multiple-pass fabrication caused some regions within the microstructure to be melted and solidified more than once. Figure 34(b) shows an interpass boundary region at higher magnification where the direction of solidification within the two passes is perpendicular. In this region ferrite is confined to the center of dendrite cores where the solidification mode would appear to be the ferrite-austenite mode (F/A mode) (Brooks *et. al.* 1981, Brooks *et. al.* 1983, Brooks *et. al.* 1984, David 1981, Bain 1924), that is solidification of primary ferrite and secondary austenite through either eutectic or peritectic reaction. Following solidification, austenite growth consumed most of the ferrite. In other regions solidification apparently occurred as single-phase ferrite (F mode), followed by solid-state transformation almost entirely to austenite.

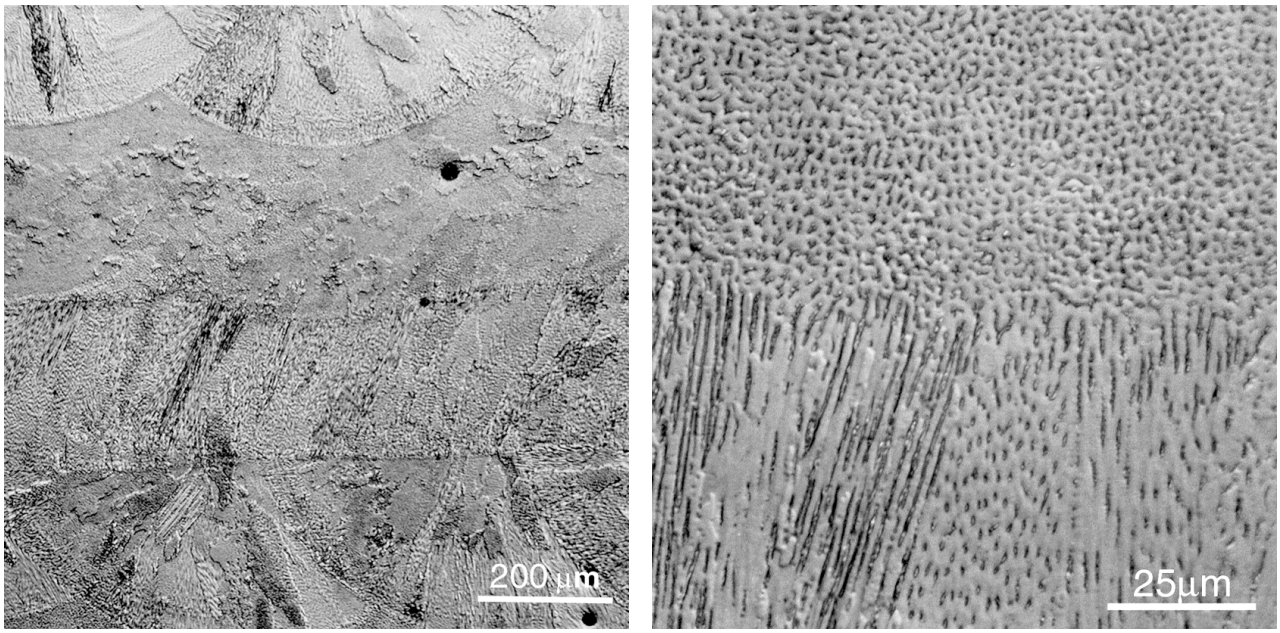

(a) (b)

Figure 34. Optical micrographs of 304L LENS-fabricated block: (a) low magnification image of passes within the layers, (b) higher magnification image at interpass boundary.

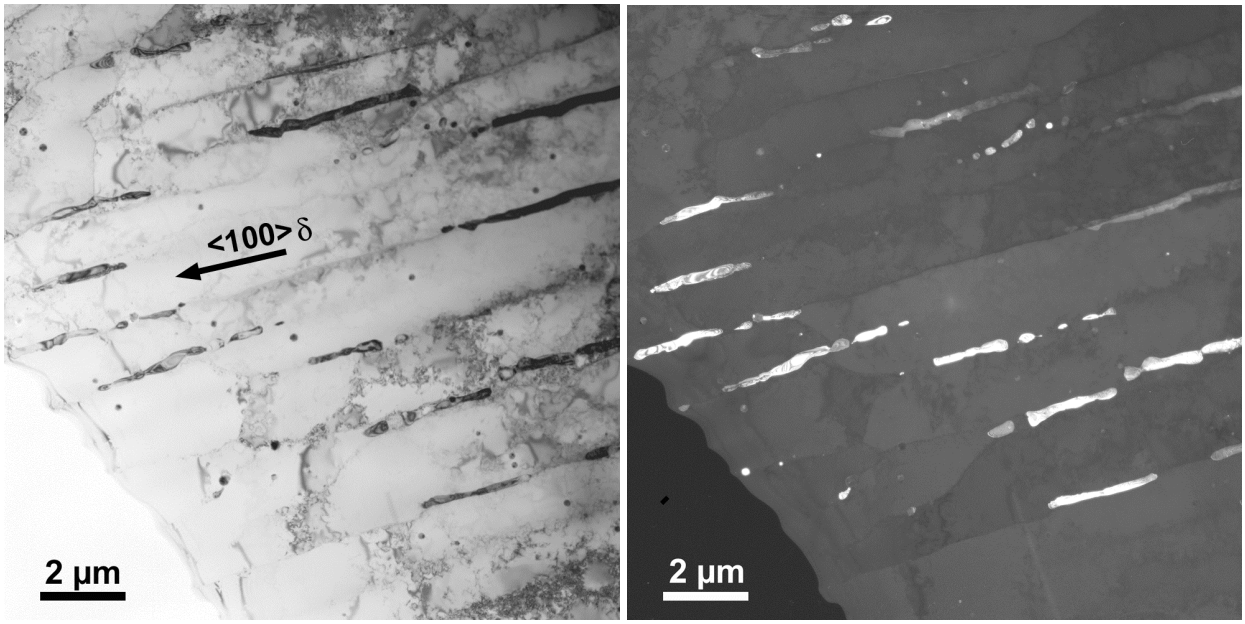

(a) (b)

Figure 35. TEM micrographs of delta-ferrite particles in dendrite cores within an austenite grain in 304L LENS-fabricated block: (a) bright field image, (b) dark field image from the 002-ferrite reflection.

Figure 35(a) is a bright-field TEM micrograph showing directionally aligned delta-ferrite particles that exhibited the new OR within one of the austenite grains. Figure 35(b) is a dark-field image from the 002-ferrite reflection that confirms all ferrite within this grain has the same crystallographic orientation. The position of solidification dendrites was revealed by the electropolishing procedure. The presence of dendritic microsegregation resulted in different electropolishing rates at dendrite cores and boundaries producing thickness oscillations in the thin foil. It can be seen that ferrite particles lie in dendrite cores and are aligned close to a $<100>_\delta$ direction, which is the normal fast-growth direction for bcc material in dendritic solidification.

Figures 36(a) and (b) show selected-area electron diffraction (SAED) patterns from one of the ferrite particles and adjacent austenite matrix in Figure 35(a). The foil normal was close to $[010]_\delta$ and the sample was tilted ± 45° about $[010]_\delta$ to obtain the two patterns. These patterns are representative of all ferrite particles in the grain. In Figure 36(a) the [-110] zone-axis pattern of austenite and [-110] zone-axis pattern of ferrite are superimposed, hence $[-110]_\gamma$ and $[-110]_\delta$ zone axes are parallel normal to the plane of the pattern. The 111_γ and 110_δ reflections are aligned within the pattern indicating that $(111)_\gamma$ planes are parallel to $(110)_\delta$ planes. Hence the OR within this grain is:

$$(111)_\gamma \,//\, (110)_\delta \text{ and } [-110]_\gamma \,//\, [-110]_\delta.$$

Likewise in Figure 36(b), $[111]_\gamma$ and $[110]_\delta$ zone-axis patterns are superimposed and -220_γ and -110_δ reflections are aligned within the pattern confirming the above OR. The parallel alignments in this new OR are summarized in Table III. The axis/angle pair description (Edington 1976) for this new OR is [-110]/35.26°, that is the bcc and fcc lattices are rotated

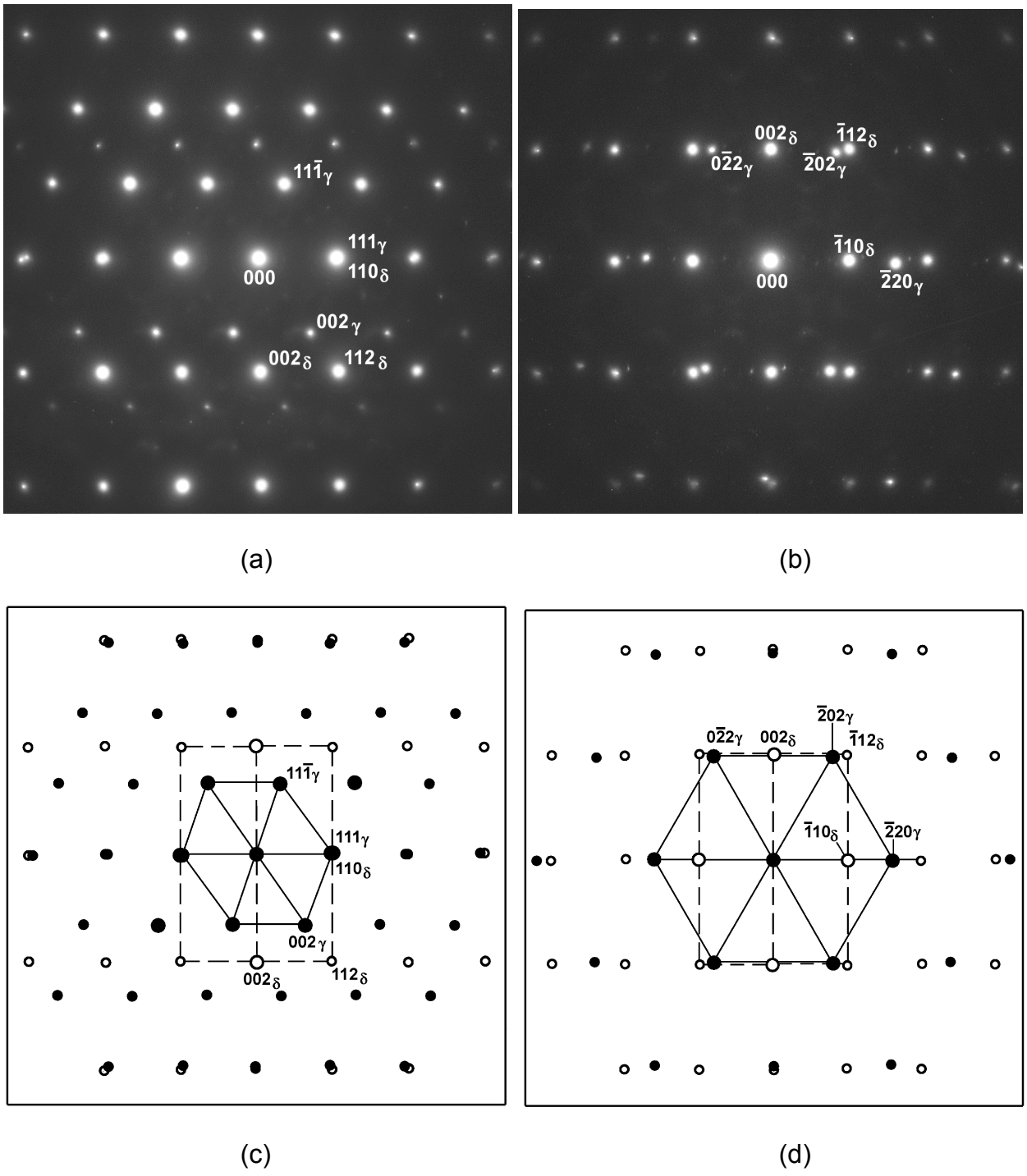

Figure 36. SAED patterns for the grain in Figure 2: (a) $[-110]_\gamma$ and $[-110]_\delta$ zone-axis patterns superimposed, (b) $[111]_\gamma$ and $[110]_\delta$ zone-axis patterns superimposed, (c) and (d) computed patterns corresponding to (a) and (b), respectively.

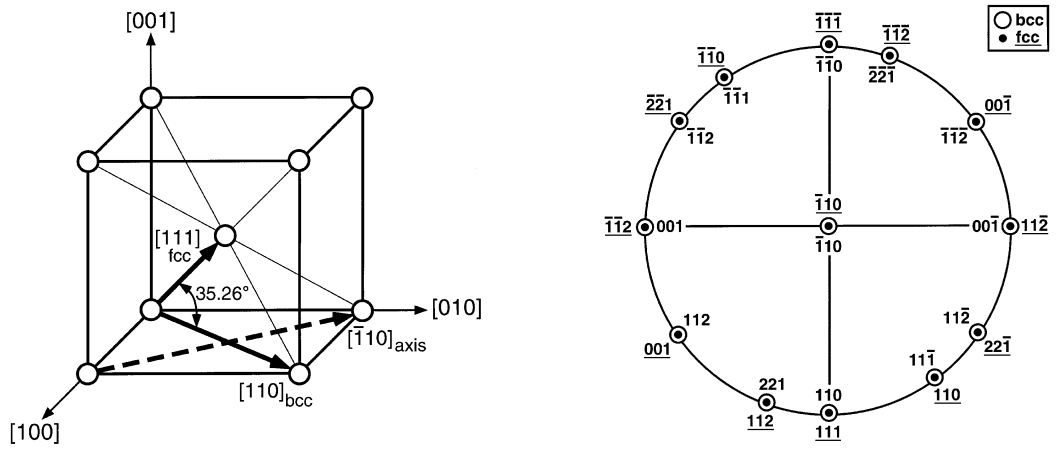

(a) (b)

Figure 37. (a) Axis-angle diagram showing the 35.26° rotation between $[111]_{fcc}$ and $[110]_{bcc}$ about the common [-110] direction that produces the new OR. (b) Composite stereogram showing the sets of coincident low-index directions generated by the new OR. Indices of fcc poles are underlined.

35.26° (the angle between [111] and [110]) relative to each other about the common [-110] direction as shown in Figure 37(a). Rotation through this angle would bring the two lattices into a cube-on-cube OR.

The sets of coincident low-index directions (and planes since both lattices are cubic) that result from this axis-angle alignment are given in column two in Table III and are shown on the composite stereogram in Figure 37(b).

Table III. Summary of Parallel Relationships in the New OR.

Name	Orientation Relationship	Close-packed Components Parallel
New OR (this study)	$(111)_{fcc}//(110)_{bcc}$, $[-110]_{fcc}//[-110]_{bcc}$ and $[11-2]_{fcc}//[00-1]_{bcc}$	c.p.-planes
	$[110]_{fcc}//[11-1]_{bcc}$ $[001]_{fcc}//[112]_{bcc}$ $[112]_{fcc}//[221]_{bcc}$ $[22-1]_{fcc}//[11-2]_{bcc}$	c.p-directions (not in the parallel c.p.-planes)

Composite SAED zone-axis patterns for the new OR were computed using a lattice parameter ratio (a_{fcc}/a_{bcc}) of 1.25 that was measured from Figure 36(a). Computed patterns corresponding to the experimental patterns in Figures 36(a) and (b) are shown in Figures 36(c) and (d), respectively. Solid and open circles correspond to austenite and ferrite reflections, respectively. Solid and dashed lines have been added to elucidate the austenite and ferrite reciprocal lattice nets. Inspection reveals a small angular difference between the experimental and computed patterns which is due to the fact that the real OR deviates slightly from the exact OR of $(111)_\gamma$ // $(110)_\delta$ and $[-110]_\gamma$ // $[-110]_\delta$. The amount of deviation in this case was measured from the projected centers of the zone axes in Figures 36(a) and (b) and found to be $(111)_\gamma$ and $(110)_\delta$ 0.7° apart, and $[-110]_\gamma$ and $[-110]_\delta$ 1.3° apart.

Another austenite grain in which the remnant delta-ferrite exhibited the new OR was found within a second TEM foil prepared from the 304L LENS-fabricated block. This grain was tilted until the beam was aligned with the coincident set of directions $[110]_\gamma$ // $[11\text{-}1]_\delta$ (see Table III and Figure 37(b). The resulting experimental and computed diffraction patterns are shown in Figures 38(a) and (b). Here $[110]_\gamma$ and $[11\text{-}1]_\delta$ zone-axis patterns are superimposed confirming that $[110]_\gamma$ // $[11\text{-}1]_\delta$ normal to the pattern, while -220_γ and -110_δ reflections are approximately aligned within the pattern. For this grain, the deviation from the exact OR is $[110]_\gamma$ and $[11\text{-}1]_\delta$ 1.8° apart, and $(-110)_\gamma$ and $(-110)_\delta$5° apart. This deviation is larger than was measured for the grain in Figures 35 and 36.

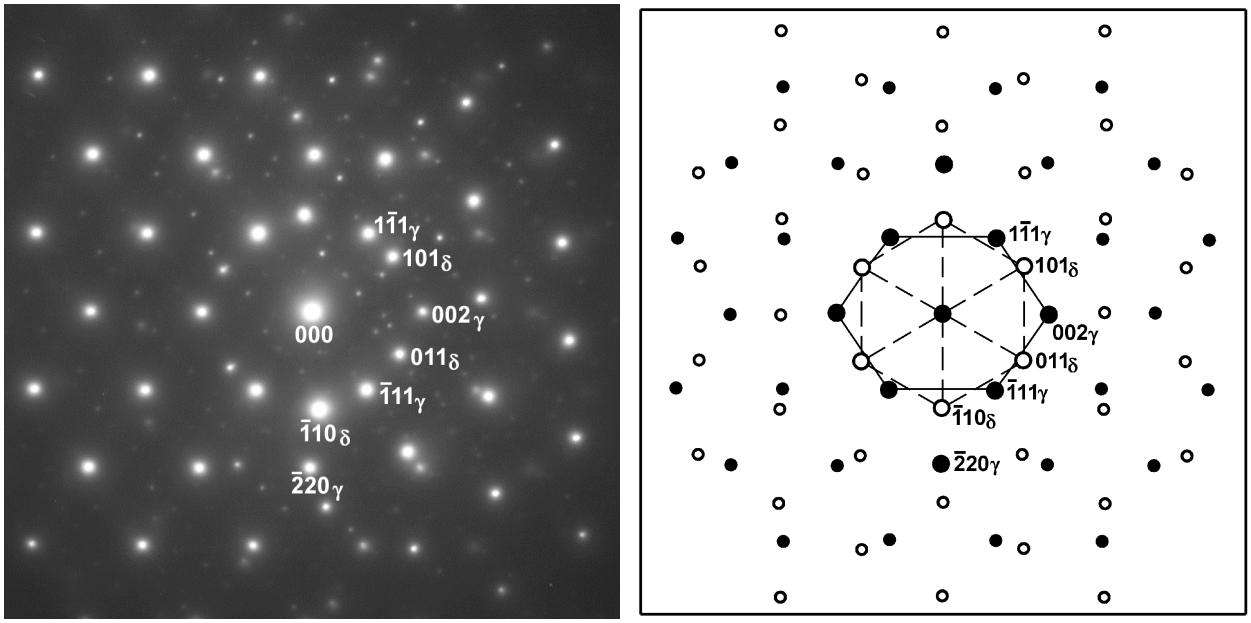

Figure 38. (a) SAED pattern for a second grain exhibiting the new OR in 304L LENS-fabricated block, $[110]_\gamma$ and $[11\text{-}1]_\delta$ zone-axis patterns superimposed weak spots in the background arise from diffraction effects at the interface. (b) Computed pattern corresponding to (a).

These two grains were the only ones found exhibiting the new OR among all grains in the thin portions of the two TEM foils from this material. In all other grains, remnant delta-ferrite resided in dendrite cores and exhibited either the K-S or N-W OR. No grains were found in which the ferrite did not have an OR with the austenite matrix.

309S GTA Weld

Figure 39(a) is an optical micrograph of the single-pass, autogenous GTA weld in alloy 309S sheet metal. Here the microstructure results from a single solidification and cooling event, unlike the multiple-pass microstructure of the 304L LENS-fabricated block. Figure 39(a) contains some regions where delta-ferrite has a classical skeletal (or vermicular) morphology with secondary branching and other regions where it has a lathy morphology. Tin-quenching of welds in this material showed that solidification occurred by F/A mode in which any OR would have been established during solidification. Figure 39(b) is a TEM micrograph of a grain in which all the delta-ferrite had a more skeletal-appearing morphology and exhibited the new OR with the austenite matrix. The experimental diffraction pattern for ferrite/austenite in this grain is shown in Figure 39(c) and is similar to the pattern in Figure 38(a). The $[110]_\gamma$ and $[11\text{-}1]_\delta$ zone-axis patterns are superimposed and the -220_γ and -110_δ reflections are nearly aligned within the pattern. The deviation from the exact OR is $[110]_\gamma$ and $[11\text{-}1]$ 3.5° apart normal to the pattern, and $[-110]_\gamma$ and $[-110]_\delta$ 1° apart in the plane of the pattern. Ferrite in several other grains that were thin enough to analyze in this foil did not have an established OR with the austenite matrix. No grains were found containing K-S or N-W oriented ferrite within the thin region of the foil.

Fe-Cr-Ni Alloy GTA Weld

Figure 40(a) is a TEM micrograph of the single-pass, autogenous GTA weld in the ternary Fe-Cr-Ni alloy showing delta-ferrite with a classical skeletal (or vermicular) morphology in the austenite matrix. All ferrite within this grain had a skeletal morphology with secondary branching and exhibited the new OR with the surrounding austenite. The solidification sequence for this grain is not certain, but this ferrite morphology is most often associated with F/A solidification mode (Brooks and Thompson 1991). The experimental diffraction pattern from this ferrite and adjacent austenite is shown in Figure 40(b) confirming the new OR. The pattern is similar to that in Figure 36(a) but viewed from the opposite direction, i.e. along $[1\text{-}10]_\gamma$ and $[1\text{-}10]_\delta$. (an alternate interpretation is that Figures 36(a) and 40(b) show two different variants of the new OR, where $(111)_\gamma$ // $(110)_\delta$ in Figure 36(a) and $(11\text{-}1)_\gamma$ // $(110)_\delta$ in Figure 40(b)). From Figure 40(b) the deviation from the exact OR was measured to be $[1\text{-}10]_\gamma$ and $[1\text{-}10]_\delta$ 2° apart normal to the pattern, and $[111]_\gamma$ and $[110]_\delta$ 3.5° apart in the plane of the pattern. This is a larger deviation than for the grain in Figure 36(a). As in the 309S GTA weld, this was the only grain found within the thin area of the foil in which the ferrite/austenite had established an OR. Ferrite in other grains examined did not appear to have an OR with the austenite matrix.

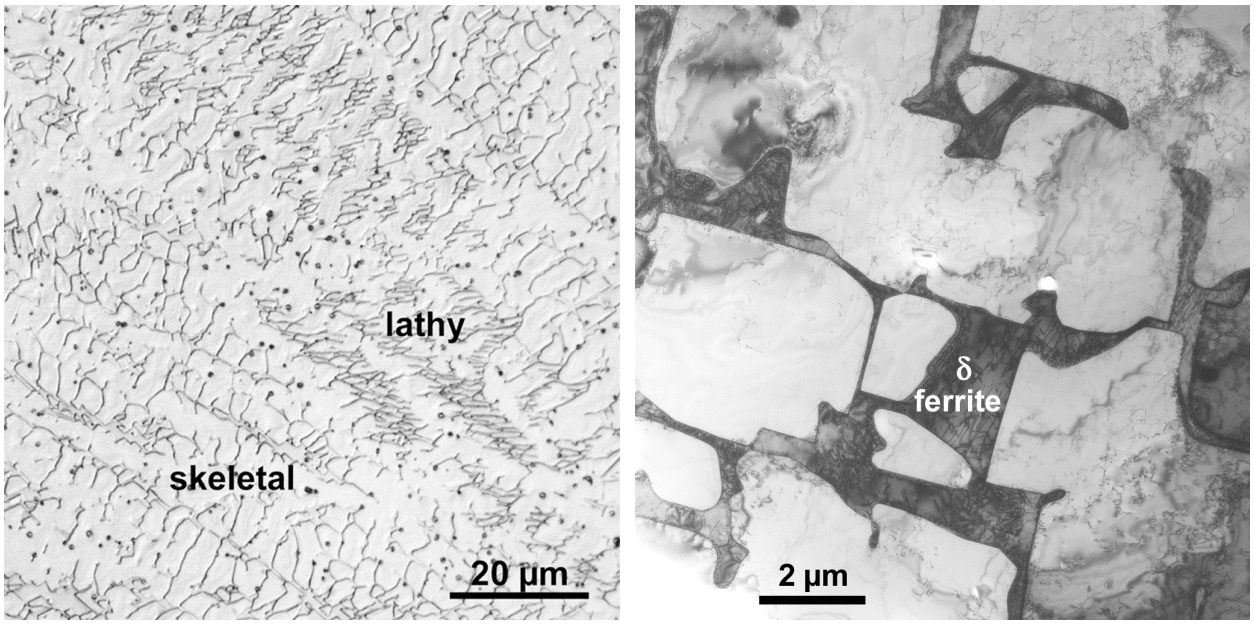

(a) (b)

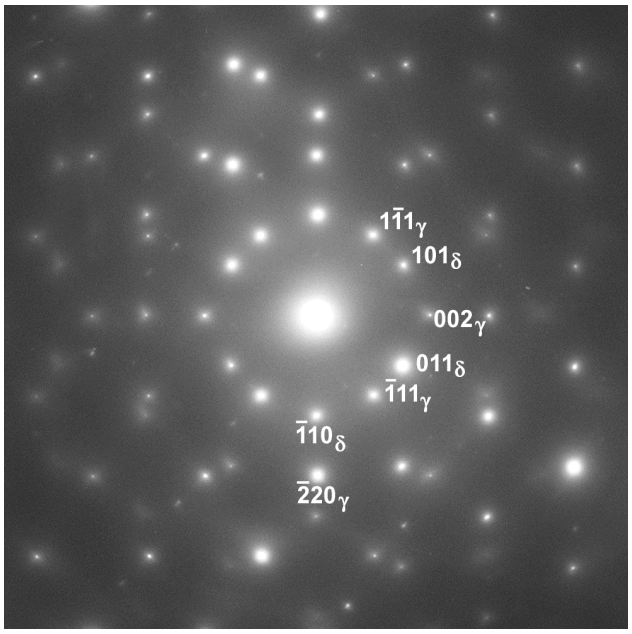

(c)

Figure 39. (a) Optical micrograph of single-pass autogenous GTA weld in 309S sheet, (b) TEM micrograph of delta-ferrite with skeletal morphology, (c) SAED pattern for (b), $[110]_\gamma$ and $[11\text{-}1]_\delta$ zone-axis patterns superimposed.

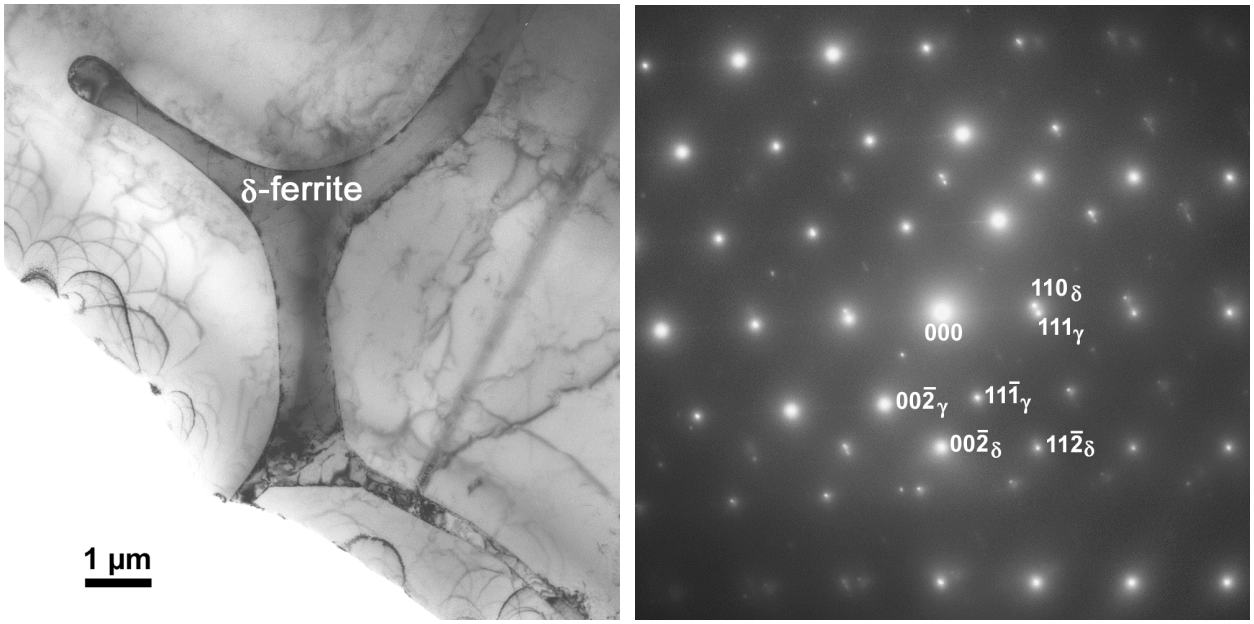

(a) (b)

Figure 40. (a) TEM micrograph of skeletal delta-ferrite in single-pass autogenous GTA weld in Fe-Cr-Ni alloy plate. (b) SAED pattern for (a), $[1\text{-}10]_\gamma$ and $[1\text{-}10]_\delta$ zone-axis patterns superimposed.

Discussion

Distinction from other Orientation Relationships

It can be seen from column two in Tables I and III that the new OR is the only one that aligns a $<110>_{fcc}$ direction parallel to a $<110>_{bcc}$ direction. This condition is not approached in any of the other bcc-fcc ORs. Column four in Table I lists the minimum angular separation between $<110>_{fcc}$ and $<110>_{bcc}$ directions. It can be seen that <110> directions in the other ORs come no closer than ~25° to alignment. This fact can be verified from inspection of composite stereograms with poles plotted for the various ORs. This $<110>_{fcc}$ // $<110>_{bcc}$ alignment provided a distinctive fingerprint in electron diffraction for distinguishing ferrite/austenite structures that had the new OR from other possible ORs. The $<110>_{fcc}$ and $<110>_{bcc}$ zone-axis patterns in electron diffraction are familiar and their superposition (e.g. Figure 36(a)) will be readily recognized when encountered in the diffraction pattern of fcc-bcc lattices with the new OR. The three different patterns in Figures 36(a), 36(b), and 38(a) or 39(c) contain this $<110>_{fcc}$ // $<110>_{bcc}$ component either normal to or within the plane of the pattern and are the most reliable diagnostic for identifying bcc-fcc structures that have the new OR. They are not similar to any patterns of superimposed low-index zones that occur in the other bcc-fcc ORs.

In a related matter, other investigators (Brooks *et. al.* 1981, Brooks *et. al.* 1983, Inoue *et. al.* 2000, Suutala *et. al.* 1979b) have frequently noted a close alignment (<10°) between <100> directions of ferrite and austenite in solidification microstructures of stainless steels. Such

alignment rules out the presence of ferrite with the new OR for which the minimum angular separation between $<100>_{fcc}$ and $<100>_{bcc}$ directions is 24.74°.

Relation to K-S and N-W Orientation Relationships

Two phases with different crystal symmetry will often adopt an OR between them where close-packed planes in each phase are parallel. Column three in Tables I and III lists the close-packed components that are parallel in the various bcc-fcc ORs. It can be seen that close-packed planes are parallel in the K-S, N-W, and new ORs. Only the K-S OR also aligns close-packed directions within those planes. The new OR does align a pair of close-packed directions, $[110]_{fcc}//[11\text{-}1]_{bcc}$, but they do not lie in the parallel close-packed planes, $(111)_{\gamma} // (110)_{\delta}$.

Dahmen (Dahmen 1982) has elucidated the rotations relating the Bain, N-W, K-S, G-T, and Pitsch ORs to one another. Here we utilize his graphical approach to show the rotations relating the new OR to the K-S and N-W ORs, each of which has a set of close-packed planes parallel. Figure 41 shows the atomic arrangements in the close-packed planes superimposed as they are aligned in the three ORs. Open and solid circles depict atoms in the $\{110\}_{bcc}$ and $\{111\}_{fcc}$ planes, respectively. Lines forming rectangles and hexagons show the two-fold and six-fold rotational symmetry of the individual two-dimensional nets. Figure 41(a) shows the atomic alignment for the N-W OR. The 2-dimensional symmetry of the combined nets is mm2. One mirror plane is normal to $[001]_{bcc} // [\text{-}101]_{fcc}$ and the other is normal to $[\text{-}110]_{bcc} // [\text{-}12\text{-}1]_{fcc}$. The close-packed directions are misaligned by 5.26°. A relative rotation of one lattice through 5.26° about the normal brings one set of close-packed directions into alignment as shown in Figure 41(b). This is the atomic alignment for the K-S OR. The two-dimensional symmetry of the overall pattern is lower as it no longer contains mirror planes. Figure 41(c) shows the alignment for the new OR. In this case, the overall pattern symmetry once again is mm2. One mirror plane is normal to $[001]_{bcc} // [\text{-}1\text{-}12]_{fcc}$ and the other is normal to $[\text{-}110]_{bcc} // [\text{-}110]_{fcc}$. Thus, alignment of $[\text{-}110]_{bcc}$ and $[\text{-}110]_{fcc}$ directions in the new OR introduces mirror plane symmetry into the atomic alignment in the close-packed planes.

Figure 42 shows composite stereograms for the three ORs projected normal to the close packed planes and oriented to match Figure 41. Open and solid circles represent bcc and fcc poles, respectively. Indices for fcc poles are underlined. Rectangles and hexagons in the stereograms show the relative orientations of the atomic nets in Figure 41. It can be seen from Figures 42(a) and (b) that a relative rotation of 5.26° about the normal to the parallel closed-packed planes will bring the N-W OR into coincidence with the K-S OR, or vice versa. (The relative rotations relating the N-W to the Bain OR and K-S to the Pitsch OR are also shown after Dahmen (Dahmen 1982)). In like manner, comparing Figure 42(c) to Figures 42(a) and (b) shows that a relative rotation of either 30° or 35.26° about the normal to the parallel closed-packed planes will bring the new OR into coincidence with either the N-W or K-S OR, respectively. Thus the new OR is related to N-W and K-S ORs by relative rotations about the normal to the close-packed planes.

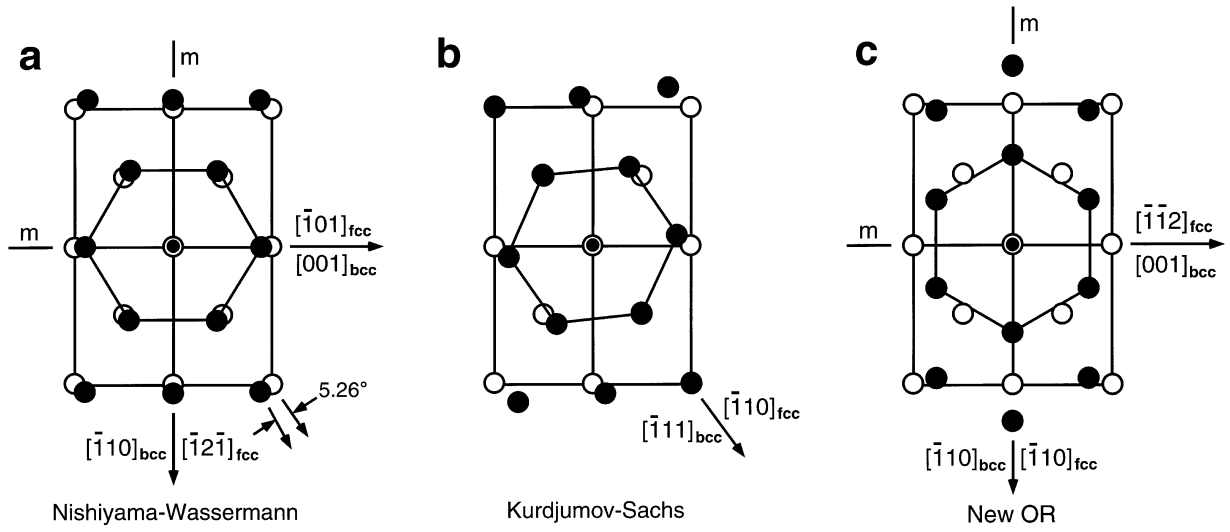

Figure 41. Atomic arrangement in close-packed planes for bcc- (open circle) and fcc- (solid circle) lattices as they are superimposed in (a) N-W OR, (b) K-S OR, and (c) the new OR. In (a) and (c), m denotes the position of mirror planes in the 2-D pattern symmetry, while arrows and indices denote real-lattice directions normal to the mirror planes. [(a) and (b) after Dahmen (Dahmen 1982)].

Deviation from Exact Orientation

The measured deviations from the exact $(111)_\gamma$ // $(110)_\delta$ and $[-110]_\gamma$ // $[-110]_\delta$ OR are tabulated in Table IV for those grains found to exhibit the new OR in this study. The range of deviation is ~1-5°. Experimental error for these measurements is estimated to be 0.5°. It should be noted also that the magnitude of this deviation varied up to ~1° with location throughout a given grain, which is typical of the amount of misorientation within a grain resulting from dendritic solidification. By comparison, both K-S and N-W oriented ferrite in the LENS-fabricated 304L block also deviated from the exact ORs but with more limited range, typically <2° for N-W oriented ferrite and ~1° for K-S oriented ferrite. For example Figure 43(a) shows the experimental diffraction pattern for ferrite oriented ~1.1° from exact N-W orientation in the LENS-fabricated 304L block. Figure 43(b) is the corresponding computed pattern for the exact N-W OR.

Table IV. Measured deviations from exact OR.

Sample	Grain #	$(111)_\gamma$ and $(110)_\delta$	$[-110]_\gamma$ and $[-110]_\delta$
304L-2 Lens block	1	0.7 ° apart	1.3 ° apart
	2	1.8 ° apart	5 ° apart
309S-4A GTA weld	1	3.5 ° apart	1 ° apart
Fe-Cr-Ni GTA weld	1	3.5 ° apart	2 ° apart

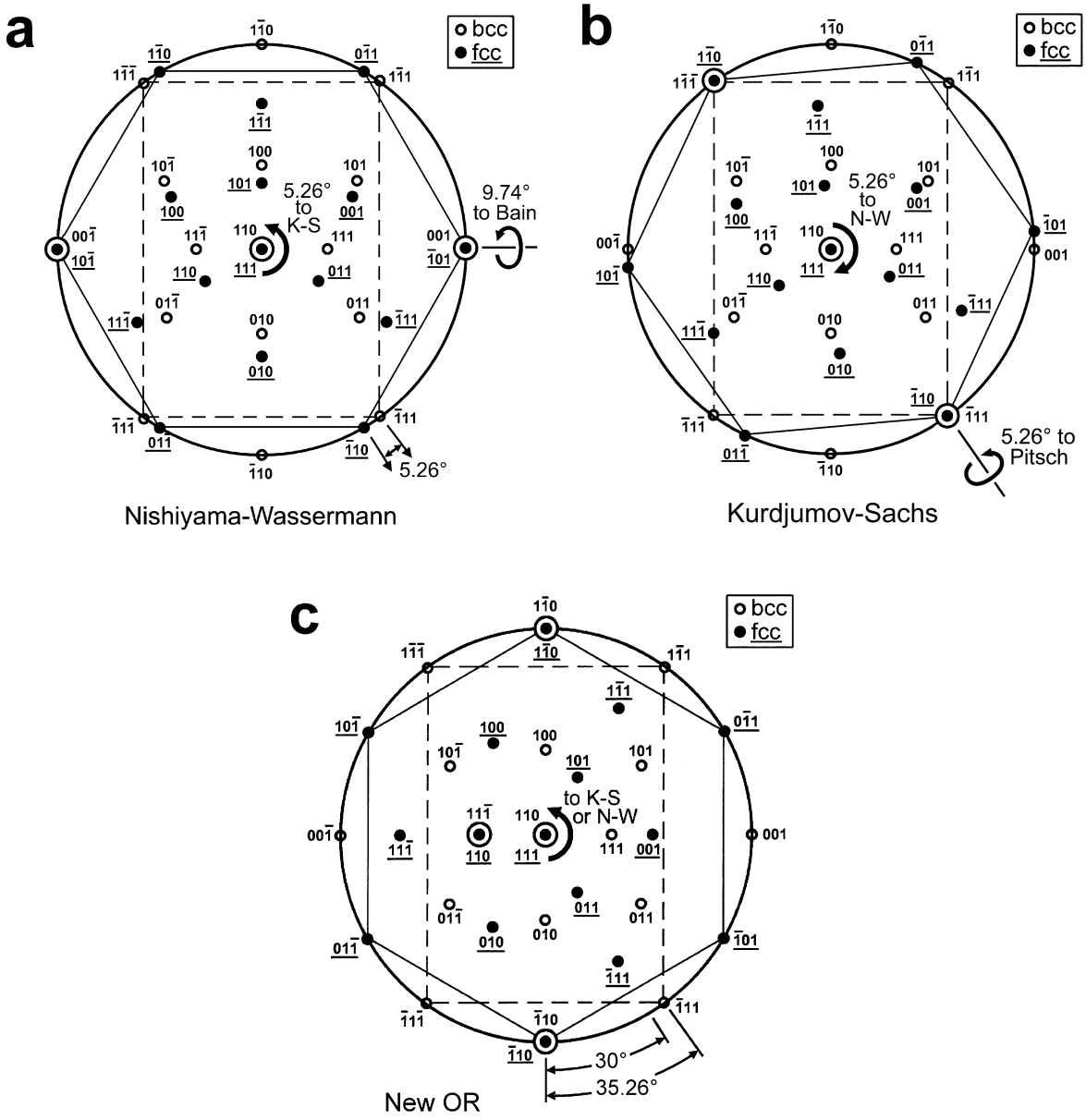

Figure 42. Composite stereograms projected normal to the close-packed planes for (a) N-W OR, (b) K-S OR, and (c) the new OR, oriented to match Figure 41. Open and solid circles represent bcc and fcc poles, respectively. Indices for fcc poles are underlined. Relative rotations about the projected normal ($[111]_{fcc}$ // $[110]_{bcc}$) relate the three ORs to each other. [(a) and (b) after Dahmen (Dahmen 1982)].

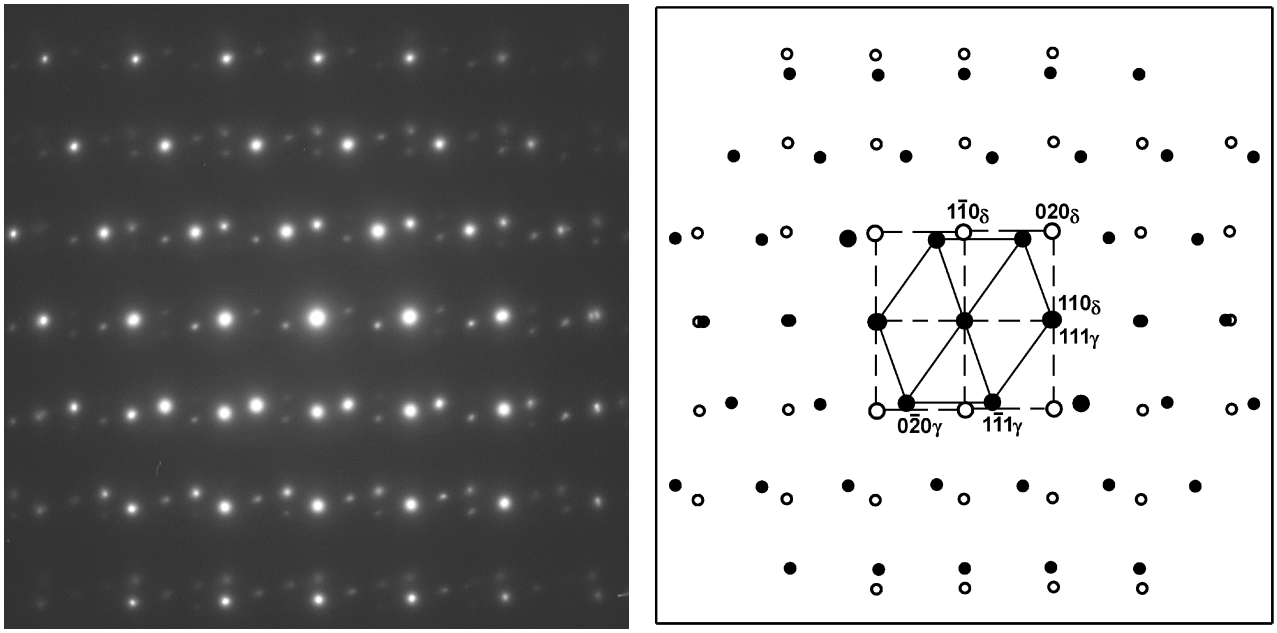

(a) (b)

Figure 43. (a) SAED pattern for a grain containing N-W oriented delta-ferrite in 304L LENS-fabricated block, $[-101]_\gamma$ and $[001]_\delta$ zone-axis patterns superimposed, (b) computed pattern corresponding to (a). Extra spots in (a) arise from double diffraction.

Frequency of Occurrence

We observed a total of four grains exhibiting the new OR in the three materials investigated by TEM in this study. This number represents a relatively small proportion of the total number of grains (~ 40) within the collective thin area of the four TEM foils examined. Therefore, one must consider if the orientations within these four grains resulted merely from coincidental alignment. First we consider an infinite number of grains having a *completely* random set of coincidental orientations between ferrite and austenite. This set contains only a very small subset (~ 0.3%) whose orientations lie within the ± 5° range of deviation from the exact new OR that was observed in this study. It is highly unlikely that we would have encountered as many as four grains out of 40 with this orientation if they were a result of random alignment. Secondly, a more restricted case of coincidental alignment should be considered. Inoue et. al. (Inoue et. al. 2000) recently reported in certain austenitic stainless steel welds that, depending on welding heat source direction, some ferrite established a K-S OR, other ferrite established only a parallel relationship between <100> directions with austenite, and still other ferrite established only a parallel relationship between close-packed planes with austenite. We consider the latter case where a set of close-packed planes is parallel between the two lattices but the relative orientation within those planes may be random. Then the subset of chance grains whose orientations lie within the ± 5° range of deviation from the exact new OR is the ratio of 20° to 360°, or about one grain in 18. (We double the ± 5° range in this ratio because the diffraction patterns for positive and negative zone axes will appear to give the same OR). In the

present case of the 304L LENS-fabricated block, most grains contained either K-S or N-W oriented ferrite. The only exceptions were the two grains with the new OR. This result is inconsistent with one grain in 18 chance alignment. We conclude that the occurrences of the new OR found in this study were not coincidental alignments.

Formation of the New Orientation Relationship

Our evidence suggests that the new OR observed between delta-ferrite and austenite in this study was established during solidification rather than in the solid state. The structures examined here solidified largely in F/A-mode where a large fraction of the liquid solidifies as primary ferrite followed by secondary solidification of the remaining liquid as austenite. The 309S GTA weld was shown through tin quenching to solidify in F/A mode, apparently by peritectic reaction. The Fe-Cr-Ni alloy GTA appeared in optical microscopy to have solidified in mixed mode with most grains solidifying in F/A mode but with some solidifying in A/F mode (as primary austenite with secondary ferrite). Although the LENS-fabricated 304L material underwent multiple fusion and solidification events during sequential passes, detailed STEM profiles revealing the nature of dendritic microsegregation and ferrite confined totally to dendrite cores indicated that most regions of this sample also solidified in F/A mode during the final pass.

Thus most, if not all, of the structures that exhibited the new OR in this study were formed during F/A-mode solidification. The new OR would then be established *during* solidification as secondary austenite nucleates on primary ferrite. In this case, it is likely that bulk strain energy would be minimal or nonexistent and nucleation would be controlled primarily by the volume and interfacial energies. This may be in part why the new OR has not been observed for solid-state crystallographic transformations in which the strain energy component is significant, e.g. the martensitic transformation. Similarly, Clarke and Stobbs (Clarke and Stobbs 1974) suggested that the lack of accompanying strain during solidification may be why the distribution of ORs between bcc-chromium and fcc-copper phases in a unidirectionally solidified Cu-Cr eutectic alloy were not intermediate between K-S and N-W ORs as expected. In the absence of significant bulk strain during solidification, the magnitude of the interfacial energy may control selection of a given OR between phases. Furthermore, since the K-S and N-W ORs occur far more frequently in F/A solidified structures of ferrite and austenite, the interfacial energies associated with those two ORs may be somewhat lower than that for the new OR. It is not clear what role, if any, subsequent growth may play on the final statistical distribution. Computational simulations of the interfacial energies for these three ORs would add further insight as to their statistical occurrence during solidification. Similarly, computational studies would add insight as to whether the new OR could be established in solid-state transformation at high temperature where the bulk strain energy component may be reduced.

Conclusions

A TEM investigation of solidification microstructures in LENS-fabricated 304L stainless steel and GTA welds in 309S stainless steel and a ternary Fe-Cr-Ni alloy led to the observation of a new OR between delta-ferrite and austenite within some grains. Evidence for this new OR was obtained from SAED patterns. This new OR has not been previously reported for bcc-fcc systems. The following conclusions can be drawn from this work.

1. The new OR is $(111)_{fcc}$ // $(110)_{bcc}$ and $[-110]_{fcc}$ // $[-110]_{bcc}$. The $<110>_{fcc}$ // $<110>_{bcc}$ alignment is distinctive among known bcc-fcc ORs. This fact that may be utilized in electron diffraction analysis to distinguish the new OR from other known ORs in bcc-fcc microstructures. The diagnostic zone-axes patterns are $[-110]_{fcc}$ // $[-110]_{bcc}$, $[111]_{fcc}$ // $[110]_{bcc}$, and $[110]_{fcc}$ // $[11-1]_{bcc}$.

2. A set of close-packed planes is parallel between bcc and fcc lattices in the new OR but close-packed directions are not parallel. Since close-packed planes are parallel, the new OR is related to the well-known K-S and N-W ORs by relative rotations about the normal to the parallel close-packed planes. Rotations of 35.26° and 30° bring the New OR into coincidence with the K-S and N-W ORs, respectively.

3. The frequency of occurrence of ferrite/austenite with this new OR was quite low for the steel compositions and specific solidification/cooling conditions investigated in this study. It was observed in a total of two grains in the LENS-fabricated 304L stainless steel, and in one grain each in the GTA welds of 309S stainless steel and the ternary Fe-Cr-Ni alloy.

4. The new OR observed in this study is believed to have been established during F/A-mode solidification where the bulk strain energy during nucleation of secondary austenite on primary ferrite is likely minimal. The relative magnitude of the interfacial energy is then suggested to be controlling selection of a given OR between the two phases and hence has a major influence on the statistical distribution of ORs observed in the solidified microstructures.

References for Orientation Studies

Bain, E., 1924, *Trans. Metall. Soc. A.I.M.E.*, vol. 70, pp. 25-46.

Barrett, C. S., and Massalski, T. B., 1966, *Structure of Metals*, 3rd ed.,McGraw-Hill Book Co., New York, NY, pp. 520-525.

Brooks, J. A., and Thompson, A. W., 1991, *Int. Mater. Rev.*, vol. 36, pp. 16-44.

Brooks, J. A., Williams, J. C., and Thompson, A. W., 1981, *Proc. Conf. on Trends in Welding Research in the United States*, S. A. David, ed., ASM International, Metals Park, OH, pp. 331-357.

Brooks, J. A., Williams, J. C., and Thompson, A.W., 1983, *Metall. Trans. A*, vol.14A, pp.1271-1281.

Brooks, J. A., Yang, N. C. Y., and Krafcik, J. S., 1992, *Proc. Conf. on Trends in Welding Research in the United States*, S. A. David, ed., ASM International, Metals Park, OH, p. 173-180.

Brooks, J. A., Thompson, A. W., and Williams, J. C., 1984, *Weld. J.*, *Res. Suppl.*, vol. 63, pp. 71s-83s.

Clarke, D. R., and Stobbs, W. M., 1974, *Metal Science*, vol. 8, pp. 242-246.

Dahmen, U., 1982, *Acta Metall*., vol. 30, pp. 63-73.

David, S. A., 1981, *Weld. J., Res. Suppl*., vol. 60, pp. 633s-71s.

Edington, J. W., 1976, *Practical Electron Microscopy in Materials Science*, Van Nostrand Reinhold Co., New York, NY, pp. 68-72.

Greninger, A. B., and Triano, A. R., 1949, *Metals Trans*., vol. 185, pp.590-598.

Griffith, M. L., Keicher, D.M., Atwood, C.L., Romero, C.L., Smugeresky, J.E. , Harwell, L.D., and Green, L.D., 1996, *Proc. Symp. on Solid Freeform Fabrication*, Univ. of Texas Publishers, Austin , TX, p. 125.

Inoue, H., Koseki, T., Ohkita, S., and Fuji, M., 2000, *Sci. Tech. Weld. Joining*, vol. 5, pp. 385-396.

Inoue, H., Koseki, T., Ohkita, S., and Fuji, M., 1997, *Weld. Inter*., vol. 11, pp. 937-949.

Inoue, H., Koseki, T., Ohkita, S., and Fuji, M., 1998, *Weld. Inter*., vol. 15, pp. 282-296.

Kurdjumov, G., and Sachs, G., 1930, *Z. Phys*., vol. 64, pp. 325-343.

Nishiyama, Z., 1934, *Sci. Rep. Res. Inst*., Tohoku Univ., vol. 23, pp. 637-664.

Pitsch, W., 1959, *Phil. Mag*., vol. 4, pp. 577-584.

Shimizu, K., and Nishiyama, Z., 1972, *Metall. Trans*., vol. 3, pp. 1055-1068.

Suutala, N., Takalo, T, and Mosio, T., 1979a, *Metall. Trans. A*, vol. 10A, pp. 512-514.

Suutala, N., Takalo, T, and Mosio, T., 1979b, *Metall. Trans. A*, vol.10A, pp. 1173-1181.

Suutala, N., Takalo, T, and Mosio, T., 1980, *Metall. Trans. A*, vol. 11A, pp. 717-725.

Wasserman, G., 1933, *Arch. Eisenhuttenwes.*, vol. 16, p. 647.

Distribution

1	MS 0188	D. L. Chavez, 1011
1	MS 0834	J. E. Johannes, 9114
1	MS 0887	M. J. Cieslak, 1800
1	MS 0889	M. F. Smith
1	MS 9402	C. Cadden, 8724
1	MS 9405	R. Stulen, 8700
5	MS 0834	R. A. Roach, 9114
5	MS 0889	A. C. Hall, 1833
5	MS 1411	T. J. Headley, 1822
5	MS 9402	J. A. Brooks, 8724
5	MS 0889	C. V. Robino, 1833
2	MS 0899	Technical Library, 9616
1	MS 9018	Central Technical Files, 8945-1
1	MS 0612	Print Media, 9612